

# Thermoelastic properties and crystal structure of $\text{CaPtO}_3$ post-perovskite from 0 to 9 GPa and from 2 to 973 K

Alex Lindsay-Scott,<sup>a</sup> Ian G. Wood,<sup>a\*</sup> David P. Dobson,<sup>a</sup> Lidunka Vočadlo,<sup>a</sup> John P. Brodholt,<sup>a</sup> Kevin S. Knight,<sup>b,c</sup> Matthew G. Tucker<sup>b</sup> and Takashi Taniguchi<sup>d</sup>

<sup>a</sup>Department of Earth Sciences, University College London, Gower Street, London WC1E 6BT, England, <sup>b</sup>ISIS Facility, STFC Rutherford Appleton Laboratory, Harwell Science and Innovation Campus, Chilton, Didcot, Oxfordshire OX11 0QX, England, <sup>c</sup>Natural History Museum, Cromwell Road, London SW7 5BD, England, and <sup>d</sup>National Institute for Materials Science, Tsukuba, Ibaraki, Japan. Correspondence e-mail: ian.wood@ucl.ac.uk

$ABX_3$  post-perovskite (PPV) phases that are stable (or strongly metastable) at ambient pressure are important as analogues of PPV- $\text{MgSiO}_3$ , a deep-Earth phase stable only at very high pressure. The thermoelastic and structural properties of orthorhombic PPV-structured  $\text{CaPtO}_3$  have been determined to 9.27 GPa at ambient temperature and from 2 to 973 K at ambient pressure by time-of-flight neutron powder diffraction. The equation-of-state from this high-pressure study is consistent with that found by Lindsay-Scott, Wood, Dobson, Vočadlo, Brodholt, Crichton, Hanfland & Taniguchi [(2010). *Phys. Earth Planet. Inter.* **182**, 113–118] using X-ray powder diffraction to 40 GPa. However, the neutron data have also enabled the determination of the crystal structure. The  $b$  axis is the most compressible and the  $c$  axis the least, with the  $a$  and  $c$  axes shortening under pressure by a similar amount. Above 300 K, the volumetric coefficient of thermal expansion,  $\alpha(T)$ , of  $\text{CaPtO}_3$  can be represented by  $\alpha(T) = a_0 + a_1(T)$ , with  $a_0 = 2.37(3) \times 10^{-5} \text{ K}^{-1}$  and  $a_1 = 5.1(5) \times 10^{-9} \text{ K}^{-2}$ . Over the full range of temperature investigated, the unit-cell volume of  $\text{CaPtO}_3$  can be described by a second-order Grüneisen approximation to the zero-pressure equation of state, with the internal energy calculated *via* a Debye model and parameters  $\theta_D$  (Debye temperature) = 615(8) K,  $V_0$  (unit-cell volume at 0 K) = 227.186(3) Å<sup>3</sup>,  $K'_0$  (first derivative with respect to pressure of the isothermal incompressibility  $K_0$ ) = 7.9(8) and  $(V_0 K_0' / \gamma') = 3.16(3) \times 10^{-17} \text{ J}$ , where  $\gamma'$  is a Grüneisen parameter. Combining the present measurements with heat-capacity data gives a thermodynamic Grüneisen parameter  $\gamma = 1.16(1)$  at 291 K. PPV- $\text{CaPtO}_3$ , PPV- $\text{MgSiO}_3$  and PPV- $\text{CaIrO}_3$  have the same axial incompressibility sequence,  $\kappa_c > \kappa_a > \kappa_b$ . However, when heated,  $\text{CaPtO}_3$  shows axial expansion in the form  $\alpha_c > \alpha_b > \alpha_a$ , a sequence which is not simply the inverse of the axial incompressibilities. In this respect,  $\text{CaPtO}_3$  differs from both  $\text{MgSiO}_3$  (where the sequence  $\alpha_b > \alpha_a > \alpha_c$  is the same as  $1/\kappa_i$ ) and  $\text{CaIrO}_3$  (where  $\alpha_b > \alpha_c > \alpha_a$ ). Thus, PPV- $\text{CaPtO}_3$  and PPV- $\text{CaIrO}_3$  are better analogues for PPV- $\text{MgSiO}_3$  in compression than on heating. The behaviour of the unit-cell axes of all three compounds was analysed using a model based on nearest-neighbour  $B-X$  and  $A-X$  distances and angles specifying the geometry and orientation of the  $BX_6$  octahedra. Under pressure, all contract mainly by reduction in the  $B-X$  and  $A-X$  distances. On heating,  $\text{MgSiO}_3$  expands (at high pressure) mainly by lengthening of the Si–O and Mg–O bonds. In contrast, the expansion of  $\text{CaPtO}_3$  (and possibly also  $\text{CaIrO}_3$ ), at atmospheric pressure, arises more from changes in angles than from increased bond distances.

## 1. Introduction

For many years, it was thought that there were two major phases present throughout the whole of the Earth's lower mantle: perovskite-structured (PV)  $\text{MgSiO}_3$  and NaCl-structured

magnesio-wüstite,  $(\text{Mg,Fe})\text{O}$ . However, in 2004 it was discovered, by laser-heated diamond anvil cell (DAC) experiments, that PV- $\text{MgSiO}_3$  transforms to an orthorhombic  $\text{CaIrO}_3$ -structured 'post-perovskite' (PPV) phase at around

120 GPa (Murakami *et al.*, 2004; Oganov & Ono, 2004). This pressure is equivalent to a depth within the Earth of  $\sim 2700$  km, just above the core–mantle boundary, which has consequently led to the suggestion that PPV-MgSiO<sub>3</sub> might be the majority phase in the thin D'' seismic zone of the Earth that extends into the mantle up to  $\sim 300$  km from the core–mantle boundary. If this is the case, then the physical and chemical properties of post-perovskite are likely to dominate the dynamics of much of the core–mantle boundary region. For example, interpretation of the seismic data for D'' and modelling of the heat flow in this region will depend critically on the physical properties of PPV-MgSiO<sub>3</sub>, in particular its elastic moduli, the Clapeyron slope of the PV–PPV phase boundary, the degree of crystal alignment and its transport properties – diffusion, viscosity and thermal conductivity. Unfortunately, the properties of PPV-MgSiO<sub>3</sub> itself are very difficult to measure, as it is stable only at pressures of  $\sim 100$  GPa and cannot be quenched to ambient conditions.

The atomic arrangement in the PPV phase of MgSiO<sub>3</sub> differs greatly from that found in PV-MgSiO<sub>3</sub>, and thus one might expect that the physical properties of the two phases will also differ appreciably. The PV phase contains the three-dimensional network of corner-linked octahedra found in all perovskites. In contrast, the orthorhombic crystal structure of ABO<sub>3</sub> post-perovskites contains both corner-sharing and edge-sharing octahedra (see §2). The probable importance of PPV-MgSiO<sub>3</sub> in the core–mantle boundary region of the Earth implies that determination of its physical and chemical properties is essential to deep-Earth geoscientists. However, because of the difficulties inherent in the measurement of the physical and chemical properties of PPV-MgSiO<sub>3</sub> *per se*, it is more practical to obtain some of the experimental results required for comparison with computer simulations of PPV-MgSiO<sub>3</sub> from studies of isostructural analogues whose compressive and thermal distortion at lower temperature (*T*) and pressure (*P*) might be similar to those of MgSiO<sub>3</sub>. Ideally, such analogues should either form at atmospheric pressure or be recoverable to atmospheric pressure following high-pressure synthesis. If high pressure is required to form the material, it is of great advantage if the formation pressure does not exceed  $\sim 20$  GPa, as samples of around a few cubic millimetres in size may then be prepared using multi-anvil presses. The analogue phase that has been most studied to date is CaIrO<sub>3</sub> (Boffa Ballaran *et al.*, 2007; Lindsay-Scott *et al.*, 2007; Martin, Chapman *et al.*, 2007; Martin, Smith *et al.*, 2007; Martin, 2008; Sugahara *et al.*, 2008; Hirai *et al.*, 2009; Niwa *et al.*, 2011; Liu *et al.*, 2011), as this compound may be synthesized at atmospheric pressure (see *e.g.* Lindsay-Scott *et al.*, 2007). However, PPV-CaIrO<sub>3</sub> has a number of disadvantages as an analogue of MgSiO<sub>3</sub>, most obviously that the ratios of the ionic masses are very different and that CaIrO<sub>3</sub> may exhibit structural distortion due to the Jahn–Teller effect. CaIrO<sub>3</sub> also shows unusual behaviour in that, unlike MgSiO<sub>3</sub> (Guignot *et al.*, 2007), the response of the structure to heat is not simply the inverse of the response to pressure. Boffa Ballaran *et al.* (2007) have measured the bulk and axial incompressibilities of CaIrO<sub>3</sub> at ambient temperature, and its thermal expansion at both high

and low temperatures has been determined by Lindsay-Scott *et al.* (2007). The thermoelastic and structural properties of CaIrO<sub>3</sub> have also been studied as a function of pressure and temperature by Martin and co-workers (Martin, Chapman *et al.*, 2007; Martin, Smith *et al.*, 2007; Martin, 2008). It was found that the *b* axis, which is the most compressible, expanded most on heating, but that the thermal expansion of the *c* axis is far larger than that of the *a* axis, despite the fact that the *c* axis shortens less under pressure (see §5 and Fig. 12 for further details). Unfortunately, our understanding of the response of the CaIrO<sub>3</sub> structure to pressure and temperature is greatly hampered by the difficulty of obtaining accurate atomic coordinates and atomic displacement parameters. Even with single-crystal methods, it is difficult to obtain accurate oxygen coordinates by X-ray diffraction in the presence of iridium, and such studies have only been made at ambient *P* and *T* (Sugahara *et al.*, 2008; Hirai *et al.*, 2009). Investigations of the structure by X-ray powder diffraction have been made at high *T* (Martin, Chapman *et al.*, 2007), including a pair-distribution function study (Martin, 2008), and general trends in the oxygen coordinates are discernable but their scatter is understandably large. For such materials, containing both 'light' and 'heavy' atoms, neutron diffraction commonly offers a better method for the determination of their crystal structure, but in the particular case of CaIrO<sub>3</sub> neutron studies are greatly hampered by the very high absorption cross section of the Ir ions. The results available from the high-*P* (ambient *T*) neutron powder diffraction study of Martin, Smith *et al.* (2007) in the range 0–9.7 GPa are thus quite widely spaced in *P*, and their measurements as a function of temperature at ambient *P* are confined to data collected at 2 and 293 K.

CaPtO<sub>3</sub> (Inaguma *et al.*, 2008; Ohgushi *et al.*, 2008) is a recently reported post-perovskite analogue phase that might be expected to have some advantages over CaIrO<sub>3</sub>, although, in common with CaIrO<sub>3</sub>, its ionic mass ratios are very different from those of MgSiO<sub>3</sub> and its crystal structure is equally difficult to determine accurately by X-ray diffraction. However, unlike CaIrO<sub>3</sub>, CaPtO<sub>3</sub> does not exhibit structural distortion due to the Jahn–Teller effect and it is also far more amenable to investigation by neutron diffraction as, although not negligible, the thermal neutron absorption cross section of Pt is less than one-fortieth of that of Ir. A disadvantage of CaPtO<sub>3</sub> is that, to date, its synthesis has been reported only at high pressures, in the range from 4 (Ohgushi *et al.*, 2008) to 7 GPa (Inaguma *et al.*, 2008). After synthesis, CaPtO<sub>3</sub> is readily recoverable to atmospheric pressure, where it remains stable or at least very strongly metastable. The crystal structure of CaPtO<sub>3</sub> has been determined at ambient temperature and pressure by X-ray powder diffraction by Inaguma *et al.* (2008) and by Ohgushi *et al.* (2008), who also measured the temperature dependencies of the magnetic susceptibility and specific heat in the range 1.8–300 K. Very recently, the isothermal equation of state of CaPtO<sub>3</sub> has been determined at pressures up to 40 GPa (at ambient *T*) by synchrotron X-ray powder diffraction (Lindsay-Scott *et al.*, 2010).

In this paper, we report measurements of the thermoelastic and structural properties of CaPtO<sub>3</sub> by time-of-flight neutron

powder diffraction at the ISIS neutron source (STFC Rutherford Appleton Laboratory, England) in order to compare its behaviour with that of  $\text{CaIrO}_3$  and  $\text{MgSiO}_3$ . We have examined the material both under compression to 9.27 GPa at ambient temperature and when heated from 2 to 973 K at ambient pressure.

## 2. The PPV structure

The PPV  $\text{ABO}_3$  structure is frequently described as being composed of  $\text{BO}_6$  octahedra linked by sharing edges into chains that run parallel to  $[100]$ . These chains are then linked along  $[001]$  by sharing corners, so as to form sheets of octahedra lying parallel to  $(010)$ , which are separated along  $[010]$  by planar interlayers of  $A$  cations. These features are illustrated in Fig. 1(a), which shows the crystal structure of PPV- $\text{CaPtO}_3$  viewed down the  $a$  axis. The space group of the PPV- $\text{ABO}_3$  structure is  $Cmcm$  with  $Z = 4$ . The cell parameters of PPV- $\text{CaPtO}_3$  are  $a \simeq 3.13$ ,  $b \simeq 9.92$  and  $c \simeq 7.35$  Å at 300 K. All atoms in the structure are in special positions. The  $B$  cation is located on the  $4c$  sites  $(0, y, \frac{1}{4})$  which have site symmetry  $m2m$  (the site-symmetry symbols refer to the  $a$ ,  $b$  and  $c$  axes, respectively). For the  $A$  cation,  $y \simeq 0.25$ , and for the O1 anion, which corner links the octahedra along  $[001]$ ,  $y \simeq 0.92$ . The O2 anions, which edge link the octahedra along  $[100]$ , are located on  $8f$  sites  $(0, y, z)$  with site symmetry  $m$  (the mirror plane lying perpendicular to the  $a$  axis); for O2,  $y \simeq 0.63$  and  $z \simeq 0.05$ .

The PPV structure is often referred to in terms of the description given above, as by using this approach it is easy both to visualize the atomic arrangement and to compare it with the  $\text{ABO}_3$  PV structure, in which the network of  $\text{BO}_6$  octahedra is fully corner linked. However, as pointed out by, for example, Sugahara *et al.* (2008), the PPV structure can equally well be viewed as being composed of sheets of composition  $\text{AO}_3$ , also lying parallel to  $(010)$ , formed from linked  $\text{AO}_8$  coordination polyhedra (hendecahedra or undecahedra) separated by interlayers of  $B$  cations (see Fig. 1a). The  $\text{AO}_8$  hendecahedron is a polygon with eight vertices and 11 faces, formed from a trigonal prism (with two O1 anions and four O2 anions at its vertices) which is capped on two of its prism faces by O2 anions (see Fig. 1b); the axis of

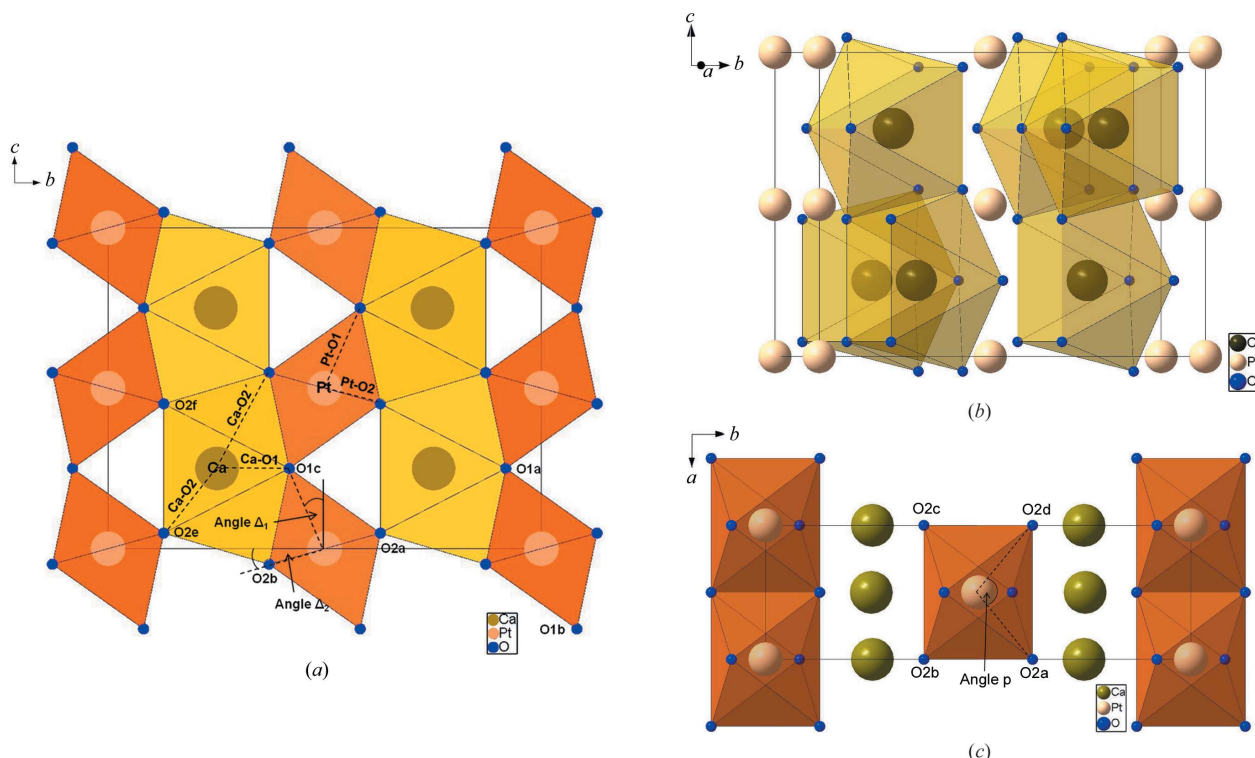


**Figure 1**

(a) The PPV- $\text{CaPtO}_3$  structure, viewed along the  $a$  axis. This structure is commonly described in the following way. Rods of edge-shared octahedra running parallel to the  $a$  axis are linked into corrugated sheets by corner sharing parallel to the  $c$  axis, so as to produce sheets of  $\text{PtO}_6$  octahedra lying parallel to  $(010)$ . These sheets are then separated along the  $b$  axis by planar interlayers of  $\text{Ca}$  ions. The O atoms involved in corner linking of the octahedra are labelled O1 and those involved in edge linking of the octahedra are labelled O2. Bonds, O—O distances and tilt angles referred to in the text are shown as dashed lines. Alternatively, the structure can be pictured in terms of sheets of hendecahedral  $\text{CaO}_8$  coordination polyhedra (shown in a lighter colour). These hendecahedra are composed of triangular prisms (with the axis of the prism running parallel to the  $a$  axis), capped on two of the three prism faces, and linked into sheets (sheet composition  $\text{CaO}_3$ ) by face sharing along the  $a$  axis and edge sharing along the  $c$  axis (for further details, see text). (b) The  $\text{Ca}$  coordination polyhedra, viewed at an angle of  $20^\circ$  to  $[100]$ . Void space not occupied by the hendecahedra or octahedra forms  $\sim 37\%$  of the unit-cell volume. (c) The structure viewed along  $[001]$ , showing the coplanar ions O2a, O2b, O2c and O2d and the angle  $p$  made by O2a—Pt—O2d. The PPV structure is conventionally defined by the three unit-cell parameters,  $a$ ,  $b$  and  $c$ , and four variable atomic coordinates,  $\text{Ca } y$ ,  $\text{O1 } y$ ,  $\text{O2 } y$  and  $\text{O2 } z$ . However, it may also be defined by four bond lengths, Pt—O1, Pt—O2, Ca—O1 and Ca—O2, and three interatomic angles,  $\Delta_1$ ,  $\Delta_2$  and  $p$ , as shown in the figure.

the trigonal prism runs parallel to the  $a$  axis. These polyhedra are linked parallel to [100] by face sharing of the basal pinacoids of the trigonal prisms and are linked parallel to [001] by sharing two of the edges in each of the two caps. Both these descriptions of the PPV structure are correct but clearly neither, of itself, can be considered as providing a complete view of the interactions within the crystal structure, as the same anions form the vertices of both the  $BO_6$  octahedra and the  $AO_8$  hendecahedra, which are intimately linked. It should also be noted that some previous authors (*e.g.* Martin, Chapman *et al.*, 2007; Bremholm *et al.*, 2011) have assumed that the unit-cell volume is equal to four times the sum of the volumes of the  $BO_6$  octahedra and the  $AO_8$  hendecahedra, but this is not correct: the void space not occupied by the hendecahedra and octahedra forms more than one-third ( $\sim 37\%$ ) of the unit-cell volume.

When considering the PPV structure, it is important to note the restrictions, or lack of them, placed on the cation coordination polyhedra by the crystal symmetry. The point-group symmetry of the  $BO_6$  octahedron is  $2/m$ , with the twofold axis running parallel to the  $a$  axis. Since this point group is centrosymmetric, the  $B$  cation is constrained to lie at the geometric centre of the anion octahedron. The O1 and  $B$  ions lie on the mirror plane and the bond distances  $B-O1a$  and  $B-O1b$  must be equal, with  $O1a-B-O1b$  (Fig. 1a) constrained to be linear (in the discussion below, we refer to the O1 ions which corner link the octahedra as the ‘apical anions’). The four O2 anions which form the remaining vertices of the octahedron (here termed its ‘central plane’) are symmetry related to each other by the twofold axis and the mirror plane. Thus, the four ions O2a, O2b, O2c and O2d shown in Fig. 1(c) are required to be coplanar and constrained to lie at the corners of a rectangle; the plane defined in this way is required to have indices  $(0kl)$  but  $k$  and  $l$  need not be rational (see below). All four  $B-O2$  bond distances must be equal, but there is no requirement for them to be the same length as the  $B-O1$  bond. The central plane of the octahedron can exhibit a ‘scissors distortion’, whereby the central plane is distorted into a rectangle; the angle  $p = O2a-B-O2d$  (Fig. 1c) then differs from  $90^\circ$ , with

$$p = 2 \tan^{-1} \left( \frac{a/2}{\{[b(O2y - 0.5)]^2 + (cO2z)^2\}^{1/2}} \right). \quad (1)$$

Finally, since the apices and central plane of the octahedron are crystallographically independent of each other, two rotation angles,

$$\Delta_1 = \tan^{-1} \left[ \frac{4b(1 - O1y)}{c} \right] \quad (2)$$

and

$$\Delta_2 = \tan^{-1} \left[ \frac{cO2z}{b(O2y - 0.5)} \right], \quad (3)$$

are needed to specify their orientations with respect to the axes of the unit cell (Fig. 1a). Symmetry requires the rotations  $\Delta_1$  and  $\Delta_2$  to operate about the  $a$  axis (Fig. 1a) but places no

other restriction upon them, and thus the  $B-O1$  bond is not required to be perpendicular to the central plane of the octahedron. The deviation from perpendicularity, defined as the angle  $q$  by Kubo *et al.* (2008), is given by  $q = \Delta_2 - \Delta_1$ ; this quantity will be pressure and temperature dependent. An alternative description of the structure to that used in the present work (*i.e.* in terms of  $\Delta_1$ ,  $\Delta_2$  and  $p$ ) may, of course, be presented using the angles  $p$  and  $q$  to specify the distortion of the  $PtO_6$  octahedron, together with the  $Pt-O1-Pt$  bond angle,  $r = (180 - 2\Delta_1)^\circ$ . It should be noted that terms such as ‘octahedral rotation’ are meaningless in the context of this structure unless they are properly defined.

The point-group symmetry of the  $AO_8$  hendecahedron is  $m2m$ , with the twofold axis running parallel to the  $b$  axis and the mirror planes lying parallel to (100) and (001). The point group  $m2m$  is polar and so the  $y$  coordinate of the hendecahedron (however defined) is not fixed, nor is there any requirement that it be related to the  $y$  coordinate of the  $A$  cation; the two may move independently of each other along [010]. However, along the  $a$  and  $c$  axes there is no freedom of movement. If the hendecahedron is considered as being formed from a bicapped trigonal prism, then the prism axis is constrained to lie parallel to the  $a$  axis, with the  $A$  cation constrained to lie half-way along the prism. The plane formed by the anions O2e, O2f and O1c (Fig. 1a) must lie parallel to (100) and these three anions must form an isosceles triangle, with the  $A$  cation, when viewed in projection on (100), lying somewhere along the perpendicular bisector of the triangle (Fig. 1a). The two  $A-O1$  bonds in the trigonal prism are therefore required to be equal in length, as are the four  $A-O2$  bonds, but there is no requirement for  $A-O1$  and  $A-O2$  to be equal. The symmetry also requires that the two O2 anions that form the caps of the prism both lie on the mirror plane parallel to (100), exactly half-way along the prism axis (Fig. 1a). The length of the  $A-O2$  bond in the trigonal prism and the distance from the  $A$  cation to the O2 anions forming the prism caps are not simply proportional to each other, as the former involves the length of the  $a$  axis and the latter does not. The structure may be described in terms of either of these two distances, but the  $A-O2$  bond in the trigonal prism is the shorter of the two and, therefore, might be considered to be more fundamental.

The unit-cell parameters may be specified in terms of the four shortest cation–anion bond lengths and the three tilt angles ( $\Delta_1$ ,  $\Delta_2$  and  $p$ ) by the following relationships:

$$a = 2(Pt - O2) \sin(p/2), \quad (4)$$

$$b = 2 \left( (Pt - O2) \cos(p/2) \cos(\Delta_2) + \{ (Ca - O2)^2 - (a/2)^2 - [(c/4) - (Pt - O2) \cos(p/2) \sin(\Delta_2)]^2 \}^{1/2} + [(Ca - O1)^2 - (a/2)^2]^{1/2} + (Pt - O1) \sin(\Delta_1) \right), \quad (5)$$

$$c = 4(Pt - O1) \cos(\Delta_1), \quad (6)$$

where the values of  $a$  and  $c$  required in equation (5) are incorporated by substitution of equations (4) and (6).

**Table 1**

Unit-cell volume, unit-cell parameters, fractional atomic coordinates and isotropic displacement parameters ( $U_{\text{iso}}$ ) for  $\text{CaPtO}_3$  as a function of pressure at 291 K.

The data were recorded in the order shown. The numbers in parentheses are estimated standard uncertainties and refer to the least-significant digits.  $U_{\text{iso}}$  values are  $\times 10^2 \text{ \AA}^2$ . The value of  $V_0$  used to calculate the second column is  $227.98 (7) \text{ \AA}^3$  (see Table 2).

Pressure (GPa)	$V/V_0$	Volume ( $\text{\AA}^3$ )	$a$ ( $\text{\AA}$ )	$b$ ( $\text{\AA}$ )	$c$ ( $\text{\AA}$ )	Ca $y$	Ca $U_{\text{iso}}$	Pt $U_{\text{iso}}$	O1 $y$	O1 $U_{\text{iso}}$	O2 $y$	O2 $z$	O2 $U_{\text{iso}}$	$\mu\text{Ah}$
0.02 (5)	0.9999	227.97 (1)	3.1264 (1)	9.9200 (5)	7.3504 (3)	0.2510 (4)	0.62 (8)	0.13 (4)	0.9185 (4)	0.57 (7)	0.6281 (2)	0.0490 (3)	0.54 (5)	1980
2.38 (7)	0.9862	224.83 (2)	3.1144 (2)	9.8565 (7)	7.3243 (5)	0.2512 (5)	0.43 (10)	0.03 (5)	0.9181 (5)	0.51 (9)	0.6284 (3)	0.0500 (4)	0.44 (7)	1320
5.07 (7)	0.9721	221.62 (2)	3.1018 (2)	9.7900 (6)	7.2979 (4)	0.2494 (5)	0.47 (9)	0.06 (5)	0.9177 (5)	0.45 (8)	0.6291 (3)	0.0494 (3)	0.45 (7)	1815
7.69 (9)	0.9593	218.71 (2)	3.0903 (2)	9.7296 (8)	7.2738 (6)	0.2502 (6)	0.01 (10)	-0.03 (7)	0.9174 (6)	0.45 (11)	0.6303 (4)	0.0486 (5)	0.49 (9)	1650
9.27 (7)	0.9514	216.90 (2)	3.0825 (2)	9.6954 (8)	7.2576 (8)	0.2485 (6)	0.54 (12)	0.10 (6)	0.9165 (5)	0.12 (9)	0.6300 (3)	0.0482 (4)	0.35 (8)	2970

### 3. Experimental method

As described by Lindsay-Scott *et al.* (2010), the  $\text{CaPtO}_3$  sample used in this study was synthesized at high pressure and high temperature using a belt-type high-pressure apparatus at the National Institute for Materials Science, Tsukuba, Ibaraki, Japan. A stoichiometric mixture of  $\text{PtO}_2$  and  $\text{CaO}$  was ground together and sealed in a Pt capsule, which was then compressed to 4 GPa, heated to 1073 K for 24 h and quenched to room temperature before slow decompression. The sample was characterized by X-ray powder diffraction at University College London and found to contain PPV- $\text{CaPtO}_3$ , with minor amounts of cubic  $\text{Ca}_3\text{Pt}_3\text{O}_4$  (Bergner & Kohlhaas, 1973) and a trace of metallic Pt [see Lindsay-Scott *et al.* (2010) for details]. Each synthesis run produced  $\sim 0.9$  g of product and so the products from three such runs were mixed together before the neutron diffraction experiments to ensure sample uniformity.

The high-pressure neutron powder diffraction patterns were collected by the time-of-flight method with the PEARL beamline high-pressure facility, HiPr (ISIS Annual Report, 1996), at the ISIS neutron source, STFC Rutherford Appleton Laboratory, England. This medium-resolution high-flux diffractometer is optimized for data collection from a Paris-Edinburgh press with opposed anvils. Nine detector modules constitute the main transverse detector bank, covering the scattering angle interval  $83 < 2\theta < 97^\circ$ , which typically yields diffraction patterns over the  $d$ -spacing range  $\sim 0.5 < d < 4.1 \text{ \AA}$  at a resolution of  $\Delta d/d \simeq 0.8\%$ . Approximately  $90 \text{ mm}^3$  of the powdered sample was loaded into an encapsulated gasket machined from null-scattering TiZr alloy, with deuterated methanol-ethanol (ratio 4:1 by volume) as the pressure-transmitting fluid, so as to provide near-hydrostatic compression (Marshall & Francis, 2002). A 2 mm polycrystalline lead pellet, placed at the centre of the sample, provided a pressure calibrant (see *e.g.* Fortes *et al.*, 2007) that could be readily separated from the sample after the experiment. Scattering into the detectors from the tungsten carbide (WC) anvils of the pressure cell was reduced by covering them with cadmium foil and by radial collimators. However, small peaks due to scattering from WC and also from the nickel binder in the anvils are still present in the diffraction patterns.

Data were collected (at ambient  $T$ ) at pressures of approximately 0, 2.4, 5.1, 7.7 and 9.3 GPa, and for counting times of between 8 and 18 h (the cumulative ISIS proton beam current in  $\mu\text{Ah}$  for each data set is shown in Table 1). After

normalization to the incident beam flux, focusing to a mean flight path and Bragg angle, and correction for detector efficiency, the logarithmically binned diffraction patterns were fitted over the range  $0.53 < d < 3.7 \text{ \AA}$  to obtain unit-cell parameters and structural data by Rietveld refinement implemented in the *GSAS* suite of programs (Larson & Von Dreele, 1994) with the *EXPGUI* graphical interface (Toby, 2001).<sup>1</sup> Five phases were included in the refinement: PPV- $\text{CaPtO}_3$ , cubic  $\text{CaPt}_3\text{O}_4$  ( $\sim 10\%$  by weight of the sample), Pb, WC and Ni. Isotropic displacement parameters were used throughout, as anisotropic displacement parameters did not improve the fit. The  $\chi^2$  values for the fits were typically 1.47, with weighted profile  $R$  factors ( $R_{\text{wp}}$ ) of typically 0.026. Examples of the fitted diffraction patterns at 0.02 and 9.27 GPa are shown in Fig. 2.

The low- and high- $T$  (ambient  $P$ ) studies were both carried out using the high-resolution powder diffractometer (HRPD) (Ibberson *et al.*, 1992) at the ISIS neutron source. This instrument, the highest-resolution diffractometer of its type ( $\Delta d/d \simeq 4 \times 10^{-4}$  in backscattering), has a total flight path of  $\sim 100$  m and three banks of detectors, with  $2\theta = 168^\circ$  ('back-scattering bank'),  $2\theta = 90^\circ$  (' $90^\circ$  bank') and  $2\theta = 30^\circ$  ('low-angle bank'). All data were collected in the time-of-flight window from 30 to 130 ms, corresponding to a  $d$ -spacing range of 0.6–2.6  $\text{\AA}$  in the backscattering detectors. The sample environment for the low- $T$  experiment (2–300 K) was an ISIS-facility He cryostat, with the powder sample, loosely packed into a rectangular aluminium-framed 'slab-can' ( $20 \times 20 \times 5$  mm) with thin vanadium windows, held under a partial pressure of 30 mbar of He exchange gas (1 bar = 100 000 Pa); the temperature stability was  $\sim \pm 0.1$  K throughout. After cooling to base temperature (2 K), data were collected for 80  $\mu\text{Ah}$  of cumulative ISIS proton beam current (equivalent to  $\sim 2.5$  h on this instrument). The sample temperature was then increased to 10 K, and thereafter in steps of 10 K to 300 K, and data were collected for 10  $\mu\text{Ah}$  of proton beam current ( $\sim 20$  min) at each temperature to allow determination of the unit-cell parameters. Data suitable for structure refinements were then collected as follows: after counting for 80  $\mu\text{Ah}$  at 300 K, the temperature was decreased to 150 K (80  $\mu\text{Ah}$ ) and then to 33 K (60  $\mu\text{Ah}$ ), after which data sets were collected in

<sup>1</sup> Supplementary data for this paper are available from the IUCr electronic archives (Reference: KS5288). Services for accessing these data are described at the back of the journal.

increments of 33 K at six temperatures to 233 K (all for 60  $\mu\text{Ah}$ ) and finally at 266 K for 100  $\mu\text{Ah}$ .

After this low- $T$  experiment, the sample was recovered for use in the high- $T$  study. To reduce the rate of decomposition of the  $\text{CaPtO}_3$  sample in the furnace vacuum, the powder sample was loosely packed in a silica glass tube of 6 mm internal diameter and 1 mm wall thickness which was then evacuated and sealed. This tube was placed in an 8 mm-diameter cylindrical vanadium sample can which was, in turn, attached to a centre stick and placed in an ISIS furnace, constructed with vanadium windings and vanadium windows. The temperature was controlled to better than  $\pm 0.2$  K throughout. Data were collected between 291 and 973 K in a series of measurements designed to minimize the possibility of sample decomposition, which was expected to occur somewhere above 873 K. Following a measurement at ambient temperature (291 K; 160  $\mu\text{Ah}$ ), data for structure refinements were collected in 100 K steps to 869 K (each counted for 160  $\mu\text{Ah}$ ). The sample was then cooled to 423 K (a lower temperature was not practicable, as the furnace responds very slowly below this temperature) and measurements were made at intervals of 25 K from 423 to 973 K (10  $\mu\text{Ah}$ ) for determination of the

unit-cell parameters. Finally, four more measurements were made on cooling the sample, all counted for 160  $\mu\text{Ah}$ : two at 973 K, followed by one at 823 K and one at 623 K.

For the HRPD experiments, data analysis was carried out with the backscattering data only ( $2\theta = 168^\circ$ ), using a  $d$ -spacing range of 0.66–2.48  $\text{\AA}$ . Inclusion of the data from the  $90^\circ$  detector bank offered little advantage as only two additional Bragg reflections were recorded. We also wished to avoid the possibility of having to introduce bank-dependent preferred orientation corrections into the refinement (see *e.g.* Fortes *et al.*, 2006). No further reflections could be seen in the low-angle bank. Preliminary refinement of the structure revealed that the absorption of the sample, when combined with the differing sample geometries in the cryostat and in the furnace, was sufficient to cause a noticeable mismatch in the refined parameters from the data sets collected at room temperature during the heating and cooling experiments. Therefore, the packing density of a similar  $\text{CaPtO}_3$  sample was measured and the *MANTID* suite of programs (Scientific Computing World, 2008; Mantid, 2010) used to calculate and apply the appropriate absorption correction for each sample environment. After normalization to the incident beam flux,

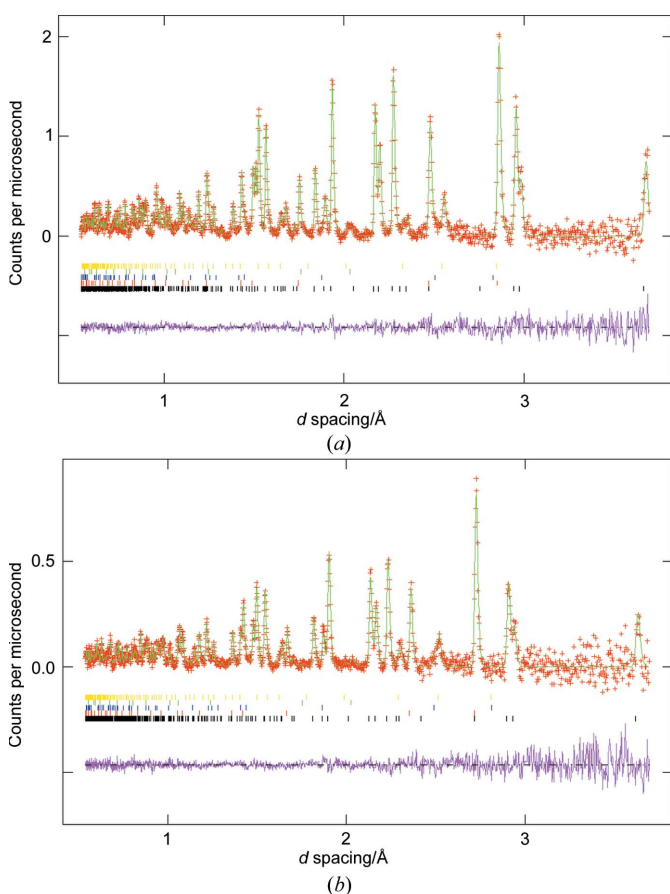


**Figure 2** Observed (points), calculated (line) and difference (lower trace) neutron powder diffraction patterns (background subtracted) for Rietveld refinements of  $\text{CaPtO}_3$  at ambient temperature and pressures of (a) 0.02 GPa and (b) 9.27 GPa. The tick marks show the positions of the Bragg reflections of (from the bottom upwards)  $\text{CaPtO}_3$ , Pb, WC, Ni and  $\text{CaPt}_3\text{O}_4$ .

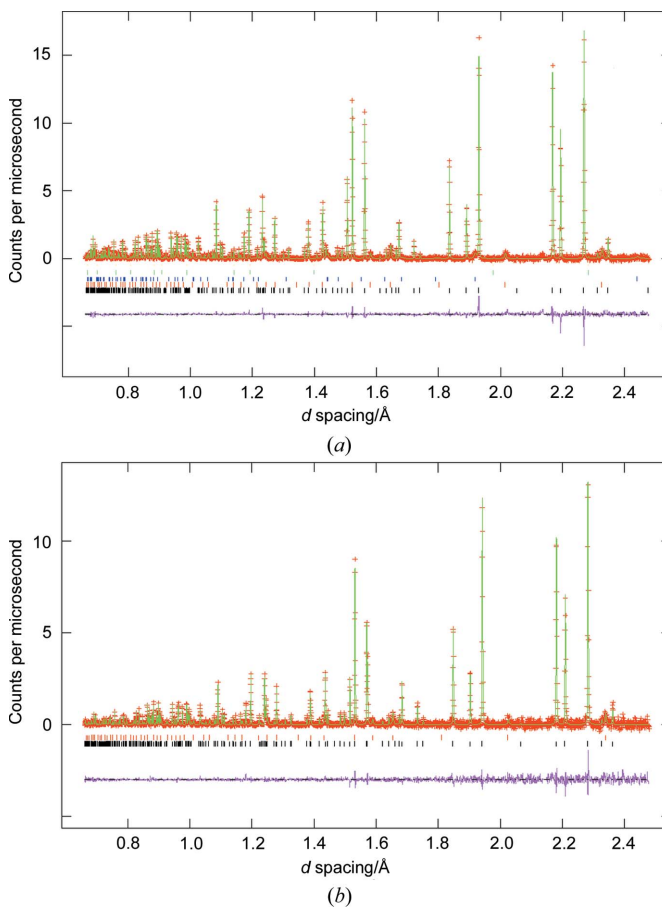


**Figure 3** Observed (points), calculated (line) and difference (lower trace) neutron powder diffraction patterns (background subtracted) for Rietveld refinements of  $\text{CaPtO}_3$  at ambient pressure and (a) 2 K and (b) 869 K. The tick marks show the positions of the Bragg reflections of (from the bottom upwards)  $\text{CaPtO}_3$  and  $\text{CaPt}_3\text{O}_4$ , and (for the 2 K refinement only)  $\text{Ca}(\text{OH})_2$  and aluminium.

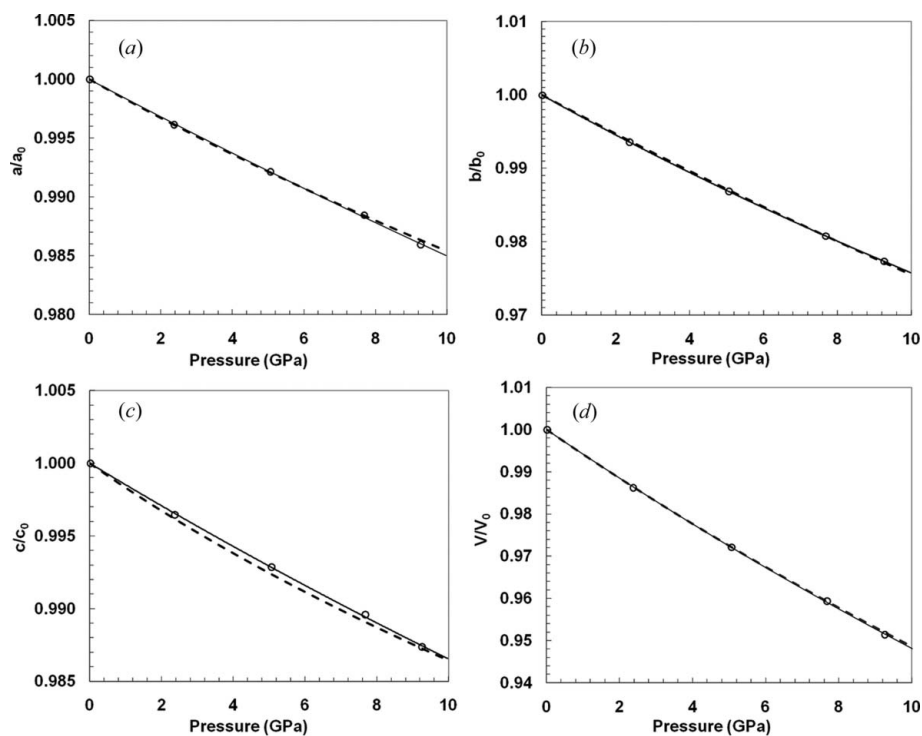


**Figure 4** Unit-cell parameters [panels (a)–(c)] and unit-cell volume [panel (d)] of  $\text{CaPtO}_3$  between 0.02 and 9.27 GPa, at ambient temperature, plotted as fractions of their values at 0 GPa as obtained from their equation of state (i.e.  $V/V_0$  etc.; see Table 2). Experimental values are shown as points; error bars are smaller than the symbols used. Solid lines show the fit of these five data points to third-order Birch–Murnaghan equations of state (see Table 2). Dashed lines show third-order Birch–Murnaghan equations of state calculated using the parameters from Lindsay-Scott *et al.* (2010) (see Table 2).

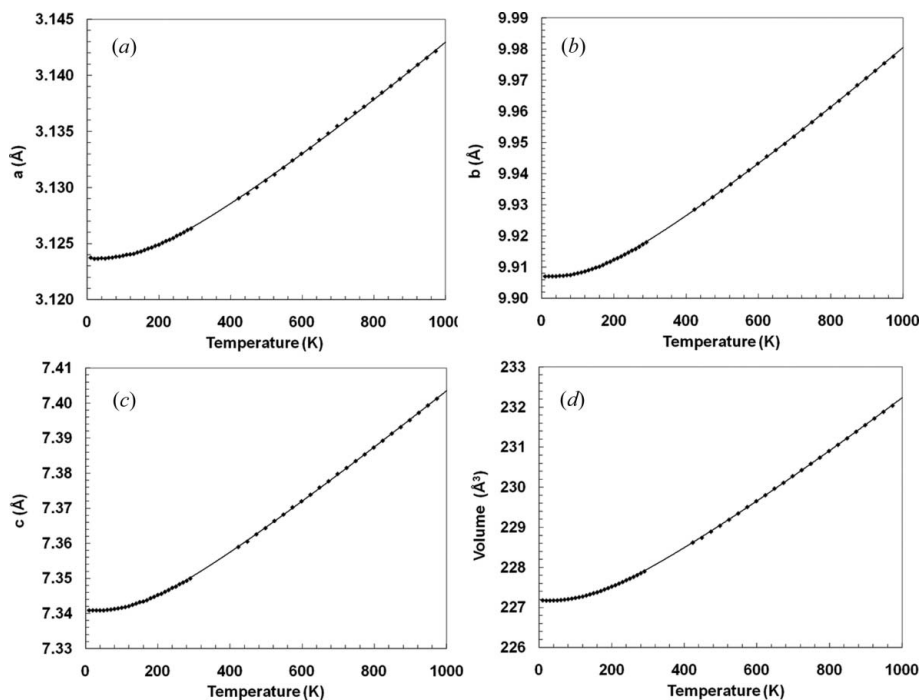


**Figure 5** Unit-cell parameters [panels (a)–(c)] and unit-cell volume [panel (d)] of  $\text{CaPtO}_3$  between 10 and 973 K, at ambient pressure. Experimental values are shown as points; error bars are smaller than the symbols used. Solid lines show the fit of the data to a second-order Grüneisen approximation to the zero-pressure equation of state (see text for details).

focusing to a mean flight path and Bragg angle, and correction for detector efficiency, the logarithmically binned backscattering data were then analysed using the *GSAS* suite of programs with the *EXPGUI* graphical interface. For data collected with short counting times (10  $\mu\text{Ah}$ ), Le Bail refinement (Le Bail *et al.*, 1988) was used to determine the unit-cell parameters. Data collected for longer times were analysed by the Rietveld method to determine the crystal structure. Four phases were included in the refinement of the data collected with the sample in the cryostat:  $\text{CaPtO}_3$  and  $\text{CaPt}_3\text{O}_4$ ,  $\text{Ca}(\text{OH})_2$  (a minor impurity from the synthesis), and aluminium from the sample environment (peaks from the latter were very weak and not distinguishable above 100 K). The same set of phases (excluding aluminium) was used for the data collected in the furnace [the peaks from the residue from  $\text{Ca}(\text{OH})_2$  were not distinguishable by 673 K, after its dissociation]. Isotropic displacement parameters were used in all refinements since, at temperatures below 673 K, the introduction of anisotropic displacements led to values that were not always positive definite for all atoms (O1 being the atom most commonly affected). However, at the three highest temperatures at which we were able to determine the structure (673, 773 and 869 K), where the atomic motions would be greatest, the Rietveld refinement was repeated using anisotropic displacement factors. Preferred orientation in the sample was modelled by an eighth-order spherical harmonic approximation; the mean texture index was 1.028 for the sample in the cryostat and 1.099 for the sample in the furnace. It was found that the last four data sets collected on cooling the sample in the furnace (two at 973 K, one at 823 K and one at 623 K) showed significant amounts of dissociation products from the  $\text{CaPtO}_3$ , and so these data were discarded. Examples of the fitted diffraction patterns for the Rietveld refinements at 2 and 869 K are shown in Fig. 3. For the data collected with the sample in the cryostat, the  $\chi^2$  values for the Rietveld fits were typically 1.90,

**Table 2**

Equation-of-state parameters obtained by fitting the data shown in Table 1 to third-order Birch–Murnaghan equations of state† (upper values in each pair).

The first line of values in each case gives the parameter as calculated from the data in the present work. The second line in each case gives the values reported by Lindsay-Scott *et al.* (2010) from X-ray diffraction (to 40 GPa) at 298 K. For the unit-cell edges, the values of  $K_0$  and  $K'_0$  are those obtained by fitting the cubes of the lengths of the unit-cell edges.

	$V_0, a_0, b_0, c_0$ (Å <sup>3</sup> , Å)	$K_0$ (GPa)	$K'_0$
Volume	227.98 (7) 228.10 (2)	169 (6) 168.2 (8)	4 (1) 4.51 (6)
<i>a</i> axis	3.1265 (3) 3.12777 (8)	206 (8) 195.7 (8)	3 (2) 6.63 (8)
<i>b</i> axis	9.9205 (15) 9.9191 (5)	118 (4) 123.3 (5)	4 (1) 2.37 (3)
<i>c</i> axis	7.3504 (7) 7.3551 (4)	223 (10) 192 (2)	5 (2) 12.2 (3)

† For comparison with the results of Martin, Chapman *et al.* (2007), the unit-cell volumes from this work were also fitted to a second-order Birch–Murnaghan equation of state. The resulting values of  $V_0$  and  $K_0$  were 227.98 (6) Å<sup>3</sup> and 169 (2) GPa, respectively (with  $K'_0$  fixed at 4).

with weighted profile *R* factors of typically 0.045; the corresponding values for the data collected using the furnace were 1.52 and 0.028, respectively. The LeBail fits gave values of  $\chi^2$  and  $R_{wp}$  of typically 0.96 and 0.076, respectively, in the cryostat and 1.11 and 0.055, respectively, in the furnace.

## 4. Results

### 4.1. The pressure dependence of the unit-cell parameters of PPV-CaPtO<sub>3</sub> at ambient temperature

The unit-cell volume and cell parameters of CaPtO<sub>3</sub> between 0.02 and 9.27 GPa are listed in Table 1 and shown in Fig. 4. The volumetric and axial data were fitted to third-order Birch–Murnaghan equations of state (Birch, 1978) by nonlinear least squares using the *EOS-FIT* program (Angel, 2000, 2001); in the case of the unit-cell axes, the cubes of their values were fitted. The weighting scheme in the refinement used weights calculated from the uncertainties both in the pressure and in the unit-cell volume and cell parameters. The resulting values of the three equation-of-state parameters for each of the four fits are listed in Table 2. The values are consistent with (but less precise than) those obtained from previous X-ray synchrotron DAC powder diffraction experiments to 40 GPa, which are also shown in Table 2 (Lindsay-Scott *et al.*, 2010). The variation between the two experiments in the axial values of  $K_0$  and  $K'_0$  may be due to the greater pressure range covered in the X-ray experiment. It can be seen from Fig. 4 and Table 2 that the compression is strongly anisotropic, being greatest for the *b* axis (*i.e.* for the direction perpendicular to the sheets of PtO<sub>6</sub> octahedra and Ca ion interlayers) and smallest for the *c* axis (*i.e.* along the chains of apex-linked PtO<sub>6</sub> octahedra).

### 4.2. The temperature dependence of the unit-cell parameters of PPV-CaPtO<sub>3</sub> at ambient pressure

To ensure comparability of counting statistics, the unit-cell parameter measurements of CaPtO<sub>3</sub> between 2 and 973 K (at

**Table 3**

Unit-cell parameters and unit-cell volume for CaPtO<sub>3</sub> as a function of temperature (ambient *P*).

All values are from Le Bail refinement of data collected for 10 μAh cumulative beam current. The numbers in parentheses are estimated standard uncertainties and refer to the least-significant digits.

Temperature (K)	Volume (Å <sup>3</sup> )	<i>a</i> (Å)	<i>b</i> (Å)	<i>c</i> (Å)
Cryostat				
10	227.179 (2)	3.12374 (2)	9.90707 (7)	7.34086 (5)
20	227.173 (2)	3.12365 (2)	9.90712 (7)	7.34088 (5)
30	227.174 (2)	3.12366 (2)	9.90711 (7)	7.34087 (5)
40	227.177 (2)	3.12370 (2)	9.90712 (7)	7.34086 (5)
50	227.178 (2)	3.12367 (2)	9.90726 (7)	7.34087 (5)
60	227.187 (2)	3.12373 (2)	9.90726 (7)	7.34102 (5)
70	227.196 (2)	3.12376 (2)	9.90748 (7)	7.34110 (5)
80	227.208 (2)	3.12383 (2)	9.90752 (7)	7.34127 (5)
90	227.222 (2)	3.12385 (2)	9.90784 (7)	7.34144 (5)
100	227.239 (2)	3.12392 (2)	9.90811 (7)	7.34163 (5)
110	227.257 (2)	3.12401 (2)	9.90836 (7)	7.34182 (5)
120	227.274 (2)	3.12405 (2)	9.90867 (7)	7.34206 (5)
130	227.299 (2)	3.12409 (2)	9.90907 (7)	7.34246 (5)
140	227.328 (2)	3.12421 (2)	9.90944 (7)	7.34282 (5)
150	227.357 (2)	3.12429 (2)	9.90989 (7)	7.34323 (5)
160	227.379 (2)	3.12443 (2)	9.91021 (7)	7.34341 (5)
170	227.412 (2)	3.12455 (2)	9.91073 (7)	7.34378 (5)
180	227.451 (2)	3.12465 (2)	9.91139 (7)	7.34433 (5)
190	227.484 (2)	3.12480 (2)	9.91177 (7)	7.34476 (5)
200	227.523 (2)	3.12490 (2)	9.91245 (7)	7.34527 (5)
210	227.556 (2)	3.12507 (2)	9.91291 (7)	7.34560 (5)
220	227.597 (2)	3.12523 (2)	9.91347 (7)	7.34616 (5)
230	227.637 (2)	3.12535 (2)	9.91411 (7)	7.34668 (5)
240	227.681 (2)	3.12549 (2)	9.91472 (7)	7.34730 (5)
250	227.722 (2)	3.12570 (2)	9.91539 (7)	7.34765 (5)
260	227.764 (2)	3.12584 (2)	9.91586 (7)	7.34833 (5)
270	227.808 (2)	3.12601 (2)	9.91659 (7)	7.34882 (5)
280	227.856 (2)	3.12621 (2)	9.91737 (7)	7.34931 (5)
290	227.901 (2)	3.12634 (2)	9.91802 (7)	7.34996 (5)
Furnace				
423	228.620 (3)	3.12904 (3)	9.92856 (10)	7.35897 (8)
448	228.740 (3)	3.12946 (3)	9.93036 (10)	7.36051 (8)
473	228.894 (3)	3.13001 (3)	9.93250 (10)	7.36258 (8)
498	229.040 (3)	3.13062 (3)	9.93456 (10)	7.36434 (7)
523	229.192 (3)	3.13116 (3)	9.93663 (10)	7.36639 (8)
548	229.348 (3)	3.13176 (3)	9.93905 (11)	7.36821 (8)
573	229.508 (3)	3.13241 (3)	9.94112 (10)	7.37028 (8)
598	229.655 (3)	3.13301 (3)	9.94329 (10)	7.37200 (8)
623	229.803 (3)	3.13350 (3)	9.94558 (11)	7.37387 (8)
648	229.968 (3)	3.13423 (3)	9.94761 (11)	7.37593 (8)
673	230.112 (3)	3.13482 (3)	9.94960 (11)	7.37772 (8)
698	230.279 (3)	3.13547 (4)	9.95192 (12)	7.37980 (8)
723	230.430 (3)	3.13607 (3)	9.95422 (12)	7.38153 (8)
748	230.589 (3)	3.13667 (3)	9.95656 (12)	7.38349 (8)
773	230.742 (3)	3.13720 (3)	9.95894 (12)	7.38536 (8)
798	230.907 (4)	3.13789 (5)	9.96122 (17)	7.38734 (11)
823	231.061 (3)	3.13846 (4)	9.96342 (13)	7.38929 (8)
848	231.222 (3)	3.13904 (4)	9.96577 (13)	7.39132 (8)
873	231.388 (3)	3.13967 (3)	9.96842 (12)	7.39317 (8)
898	231.553 (3)	3.14035 (4)	9.97070 (13)	7.39515 (8)
923	231.717 (3)	3.14094 (3)	9.97305 (12)	7.39725 (8)
948	231.883 (3)	3.14154 (3)	9.97546 (11)	7.39935 (8)
973	232.038 (3)	3.14214 (3)	9.97762 (11)	7.40127 (8)

ambient *P*), shown in Fig. 5 and listed in Table 3, were all taken from Le Bail refinements of the data sets collected for 10 μAh. The analysis of these results, presented below, uses a similar approach to that described for CaIrO<sub>3</sub> by Lindsay-Scott *et al.* (2007). Linear and volumetric thermal expansion values above room temperature in the form tabulated by Fei (1995) were obtained by fitting the data from 423 to 973 K to

**Table 4**

Volumetric and linear thermal expansion parameters for CaPtO<sub>3</sub>† (for details, see text).

	Value at $T_r$ (300 K) ( $\text{\AA}^3$ , $\text{\AA}$ )	$a_0$ ( $\text{K}^{-1}$ )	$a_1$ ( $\text{K}^{-2}$ )
Volume	227.887 (8)	$2.365 (34) \times 10^{-5}$	$5.05 (48) \times 10^{-9}$
$a$ axis	3.12607 (7)	$0.694 (22) \times 10^{-5}$	$1.10 (31) \times 10^{-9}$
$b$ axis	9.91849 (15)	$0.713 (15) \times 10^{-5}$	$2.71 (22) \times 10^{-9}$
$c$ axis	7.34978 (13)	$0.957 (17) \times 10^{-5}$	$1.25 (24) \times 10^{-9}$

† To reduce the effect of rounding errors in any subsequent calculations using these coefficients, some values in the table are reported to one more significant figure than is justified by their estimated standard uncertainty.

$$V(T) = V_{T_r} \exp \left[ \int_{T_r}^T \alpha(T) dT \right], \quad (7)$$

where  $V_{T_r}$  is the volume at a chosen reference temperature,  $T_r$  (here taken to be 300 K), and  $\alpha(T)$  is the volumetric thermal expansion coefficient, having the form

$$\alpha(T) = a_0 + a_1 T. \quad (8)$$

The resulting values of  $V_{T_r}$ ,  $a_0$  and  $a_1$  are shown in Table 4, together with the values obtained from similar fits for each of the cell parameters to determine the linear thermal expansion coefficients of the three axes of the unit cell. The values of  $a_0$  listed in Table 4 indicate that the expansion is anisotropic, and also that this anisotropy differs from that shown by CaPtO<sub>3</sub> on compression (see §5 for further discussion). On heating, the  $b$  axis expands at approximately the same rate as the volumetric (bulk) value divided by three, whilst the  $c$  axis expands faster than  $b$  and the  $a$  axis expands more slowly.

A more physically meaningful interpretation of the thermal expansion curve, encompassing its full temperature range, can be obtained using Grüneisen approximations for the zero-pressure equation of state (see *e.g.* Wallace, 1998). This approach also allows the investigation of the dynamics of the material by enabling estimates of the Debye temperature to be made. For data covering a wide temperature range, the second-order Grüneisen approximation is more appropriate than the first-order approximation (Vočadlo *et al.*, 2002) and takes the form

$$V(T) = V_0 U / (Q - bU) + V_0, \quad (9)$$

where  $Q = V_0 K_0 / \gamma'$  and  $b = (K'_0 - 1)/2$ .  $\gamma'$  is a Grüneisen parameter (assumed constant; Wallace, 1998),  $K_0$  and  $K'_0$  are, respectively, the isothermal incompressibility and its first derivative with respect to pressure at  $T = 0$ , and  $V_0$  is the volume at  $T = 0$ . The internal energy  $U$  may be calculated using the Debye approximation (see *e.g.* Poirier, 2000) from

$$U(T) = 9Nk_B T (T/\theta_D)^3 \int_0^{\theta_D/T} x^3 dx / [\exp(x) - 1], \quad (10)$$

where  $N$  is the number of atoms in the unit cell,  $k_B$  is Boltzmann's constant and  $\theta_D$  is the Debye temperature.

The solid line in Fig. 5(d) shows the result obtained from fitting the data for  $V(T)$  to equation (9) by weighted nonlinear least squares. Equation (9) has also been used to fit the data

**Table 5**

Fitted parameters for the second-order Grüneisen approximations to the isobaric equations of state of CaPtO<sub>3</sub> (for details, see text).

	$\theta_D$ (K)	$Q$ (J)	Fitted parameter ( $\text{\AA}^3$ , $\text{\AA}$ )	$b$
$V$	615 (8)	$3.16 (3) \times 10^{-17}$	$V_0 = 227.186 (3)$	3.4 (4)
$a$ axis	648 (13)	$11.37 (17) \times 10^{-17}$	$a_0 = 3.12373 (2)$	14 (2)
$b$ axis	574 (7)	$9.79 (9) \times 10^{-17}$	$b_0 = 9.90724 (4)$	12 (1)
$c$ axis	624 (10)	$7.96 (9) \times 10^{-17}$	$c_0 = 7.34100 (4)$	5 (1)

for  $a(T)$ ,  $b(T)$  and  $c(T)$  and these results are similarly shown as solid lines in Figs. 5(a)–5(c). Fig. 5 indicates that this model provides an excellent description of the behaviour of both the cell volume and the individual cell parameters over the full temperature range of the experiment. This point is further illustrated in Fig. 6, which shows the behaviour of the resulting volumetric thermal expansion coefficient of CaPtO<sub>3</sub>,  $\alpha(T)$ , obtained from

$$\alpha(T) = (1/V)(dV/dT). \quad (11)$$

The solid line in Fig. 6 gives the result obtained by differentiation of equation (9), while the points show the results from simple numerical differentiation by differences of the  $V(T)$  data. Again, the agreement is very good, with little indication in this case that neglect of anharmonicity has led to an underestimate of the thermal expansion coefficient at high temperatures (see *e.g.* Wood *et al.*, 2002).

The values of the four fitted parameters in the Grüneisen approximations for  $a(T)$ ,  $b(T)$ ,  $c(T)$  and  $V(T)$  are shown in Table 5. The Debye temperatures obtained by fitting all three of the axes and the volume are quite similar, with the sequence for the three axes being  $\theta_{Db} < \theta_{Dc} \simeq \theta_{Da}$ . The volumetric fit gives  $\theta_D$  of 615 (8) K, which is in reasonable agreement with the value of 530 K reported by Ohgushi *et al.* (2008) from measurements of the specific heat between 1.8 and 300 K. The difference between the two Debye temperatures may arise, at least in part, simply from the much wider temperature range of the present study. These Debye temperatures are similar to,

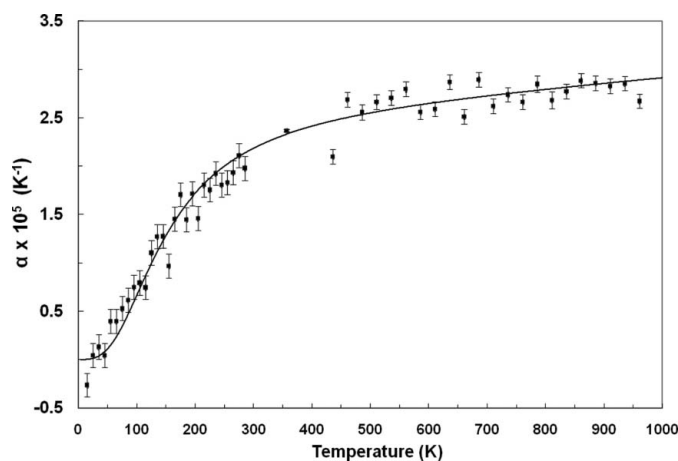


**Figure 6**

The volumetric thermal expansion coefficient of CaPtO<sub>3</sub> as a function of temperature. The points were obtained by numerical differentiation of the data shown in Fig. 5(d) and the solid line was obtained *via* equation (9).

**Table 6**

Unit-cell volume, unit-cell parameters, atomic coordinates and isotropic atomic displacement parameters ( $U_{\text{iso}}$ ) for  $\text{CaPtO}_3$  as a function of temperature (60–160  $\mu\text{Ah}$  cumulative beam current, Rietveld refinement) at ambient pressure.

$U_{\text{iso}}$  values are  $\times 10^2 \text{ \AA}^2$ .  $V_0$  was taken as the volume at 291 K. The numbers in parentheses are estimated standard uncertainties and refer to the least-significant digits.

Temperature (K)	$V/V_0$	Vol ( $\text{\AA}^3$ )	$a$ ( $\text{\AA}$ )	$b$ ( $\text{\AA}$ )	$c$ ( $\text{\AA}$ )	Ca $y$	Ca $U_{\text{iso}}$	Pt $U_{\text{iso}}$	O1 $y$	O1 $U_{\text{iso}}$	O2 $y$	O2 $z$	O2 $U_{\text{iso}}$	$\mu\text{Ah}$
Cryostat														
2	0.9967	227.173 (1)	3.12366 (2)	9.90717 (6)	7.34081 (4)	0.2512 (1)	0.39 (3)	0.23 (2)	0.9177 (1)	0.17 (3)	0.6285 (1)	0.0489 (1)	0.41 (2)	80
33	0.9967	227.174 (2)	3.12362 (2)	9.90730 (5)	7.34083 (4)	0.2515 (2)	0.47 (4)	0.43 (3)	0.9180 (2)	0.38 (3)	0.6284 (1)	0.0488 (2)	0.54 (3)	60
66	0.9968	227.189 (1)	3.12368 (2)	9.90746 (5)	7.34104 (4)	0.2515 (2)	0.36 (4)	0.25 (2)	0.9180 (2)	0.18 (3)	0.6285 (1)	0.0490 (1)	0.40 (3)	60
100	0.9970	227.234 (1)	3.12383 (2)	9.90821 (5)	7.34163 (4)	0.2513 (2)	0.41 (3)	0.26 (2)	0.9179 (2)	0.20 (3)	0.6284 (1)	0.0489 (1)	0.40 (2)	60
133	0.9973	227.304 (1)	3.12406 (2)	9.90935 (5)	7.34249 (4)	0.2514 (2)	0.39 (3)	0.22 (2)	0.9179 (2)	0.20 (3)	0.6284 (1)	0.0490 (1)	0.38 (2)	60
150	0.9975	227.352 (1)	3.12424 (1)	9.91004 (5)	7.34310 (4)	0.2515 (2)	0.42 (3)	0.28 (2)	0.9179 (1)	0.24 (3)	0.6284 (1)	0.0489 (1)	0.40 (2)	80
166	0.9977	227.399 (1)	3.12439 (2)	9.91072 (5)	7.34378 (4)	0.2512 (2)	0.45 (3)	0.25 (2)	0.9178 (2)	0.22 (3)	0.6283 (1)	0.0490 (1)	0.42 (2)	60
200	0.9982	227.517 (1)	3.12483 (2)	9.91251 (5)	7.34520 (4)	0.2512 (2)	0.47 (4)	0.26 (2)	0.9179 (2)	0.25 (3)	0.6284 (1)	0.0491 (1)	0.41 (3)	60
233	0.9988	227.645 (1)	3.12530 (2)	9.91439 (5)	7.34682 (4)	0.2515 (2)	0.49 (4)	0.25 (2)	0.9177 (2)	0.28 (3)	0.6284 (1)	0.0492 (1)	0.42 (3)	60
266	0.9994	227.789 (1)	3.12587 (2)	9.91650 (5)	7.34858 (4)	0.2510 (2)	0.58 (4)	0.26 (2)	0.9179 (2)	0.33 (3)	0.6284 (1)	0.0492 (1)	0.44 (3)	100
300	1.0001	227.949 (1)	3.12649 (1)	9.91885 (5)	7.35054 (3)	0.2512 (2)	0.62 (3)	0.23 (2)	0.9182 (2)	0.43 (3)	0.6286 (1)	0.0487 (1)	0.50 (2)	80
Furnace														
291	1.0000	227.918 (2)	3.12633 (2)	9.91857 (6)	7.35012 (4)	0.2513 (3)	0.88 (5)	0.40 (3)	0.9181 (2)	0.54 (4)	0.6285 (2)	0.0485 (2)	0.70 (3)	160
373	1.0019	228.342 (2)	3.12798 (2)	9.92472 (6)	7.35534 (5)	0.2511 (3)	1.17 (5)	0.48 (3)	0.9184 (2)	0.82 (4)	0.6284 (2)	0.0486 (2)	0.84 (3)	160
473	1.0043	228.905 (2)	3.13016 (2)	9.93278 (7)	7.36237 (5)	0.2511 (3)	1.25 (6)	0.34 (3)	0.9192 (3)	1.05 (5)	0.6289 (2)	0.0484 (2)	0.79 (4)	160
573	1.0070	229.512 (2)	3.13244 (2)	9.94128 (7)	7.37020 (5)	0.2505 (3)	1.41 (7)	0.39 (3)	0.9195 (3)	1.22 (5)	0.6286 (2)	0.0481 (2)	0.95 (4)	160
673	1.0097	230.118 (2)	3.13480 (2)	9.94984 (7)	7.37776 (5)	0.2509 (3)	1.47 (6)	0.46 (3)	0.9198 (3)	1.17 (5)	0.6281 (2)	0.0480 (2)	1.03 (4)	160
773	1.0124	230.743 (2)	3.13724 (2)	9.95882 (7)	7.38539 (5)	0.2514 (3)	1.57 (7)	0.66 (4)	0.9199 (3)	1.26 (6)	0.6277 (2)	0.0478 (2)	1.09 (4)	160
869	1.0152	231.392 (2)	3.13966 (2)	9.96858 (6)	7.39322 (5)	0.2515 (3)	1.79 (6)	0.78 (3)	0.9200 (3)	1.39 (5)	0.6276 (2)	0.0476 (2)	1.21 (4)	160

though a little lower than, that for  $\text{CaIrO}_3$ ,  $\theta_D = 703$  (11) K, obtained by fitting equation (9) to X-ray powder diffraction data (Lindsay-Scott *et al.*, 2007). Note that, by fitting a Debye model to the isobaric heat capacity data ( $C_p$ ) for  $\text{CaPtO}_3$  tabulated by Ohgushi *et al.* (2008), we obtained a slightly higher value for  $\theta_D$ , 545 (4) K, than that published, with a very similar form of misfit between the observed and calculated heat capacity curves. On converting the  $C_p$  values to their isochoric equivalents ( $C_v$ ) by means of the relationship  $C_v = C_p - \alpha^2 KVT$ , where the values of  $\alpha$  and  $V$  were taken from the present work and  $K$  from that of Lindsay-Scott *et al.* (2010), we obtained  $\theta_D = 546$  (7) K. We further found that  $C_v$  can be very well represented by a model of the internal energy with two Debye moments with different characteristic temperatures  $\theta_D^A$  and  $\theta_D^B$  constrained to the classical high-temperature limit (see *e.g.* Fortes *et al.*, 2008), *i.e.* such that

$$U(T) = 9Nk_B [Xf(\theta_D^A/T) + (1 - X)f(\theta_D^B/T)], \quad (12)$$

where  $f(\theta_D/T)$  is the Debye function and  $X$  is a mixing parameter. Using this approach, we obtained  $\theta_D^A = 199$  (45) K and  $\theta_D^B = 610$  (6) K, with  $X = 0.11$  (4). Thus, by far the greater contribution to the specific heat comes from vibrational modes whose characteristic temperature is very similar to that [615 (8) K] obtained from fitting  $V(T)$ , as described above.

The thermodynamic Grüneisen parameter,  $\gamma$ , is defined as  $\gamma = \alpha KV/C_v$ , where the specific heat at constant volume,  $C_v$ , and that at constant pressure,  $C_p$ , are related by  $C_p = C_v(1 + \alpha\gamma T)$ . By combining the thermal expansion measurements made in the present study with the value of  $K_0$  for  $\text{CaPtO}_3$  that we obtained previously (Lindsay-Scott *et al.*, 2010) and with the specific heat measurements of Ohgushi *et al.*

(2008), we obtain a value of  $\gamma = 1.16$  (1) at 291 K. This is in good agreement both with the value of  $\gamma' = 1.21$  (1) obtained from the expression  $Q = V_0 K_0 / \gamma'$ , using the data shown in Table 5 and the value of  $K_0$  from Lindsay-Scott *et al.* (2010), and with the value of the thermodynamic Grüneisen parameter at 291 K obtained within the Debye approximation from the fit to the unit-cell volume [ $\gamma = 1.23$  (3); see Wood *et al.* (2002) and equation (9) above]. These values for the Grüneisen parameter are very similar to those calculated for PPV- $\text{MgSiO}_3$  by Tsuchiya *et al.* (2005). Using density functional perturbation theory, they concluded that  $\gamma$  for PPV- $\text{MgSiO}_3$  lies in the range 1.14–1.2 at  $P = 125$  GPa and  $300 < T < 4000$  K (at this pressure, PPV- $\text{MgSiO}_3$  is stable for  $T \leq \sim 2700$  K; Tateno *et al.*, 2009). However, although equation (9) provides a reasonable estimate of both  $\theta_D$  and  $\gamma$  for PPV- $\text{CaPtO}_3$ , it is less successful at producing a correct value for  $K'_0$ ; the value for  $b$  of 3.4 (4) in Table 5 gives  $K'_0 = 7.9$  (8), which is somewhat larger than that determined by Lindsay-Scott *et al.* (2010), who found that  $K'_0 = 4.51$  (6).

In an earlier paper on the thermal expansion of PPV- $\text{CaIrO}_3$  (Lindsay-Scott *et al.*, 2007), we used a modification of equation (9) to estimate the axial incompressibilities of the material. However, later comparison with the actual axial incompressibilities determined with a DAC by Boffa-Ballaran *et al.* (2007) revealed that our estimated values were not correct. In  $\text{CaIrO}_3$ , axial thermal expansion and axial compression are not simply related to each other. For example, although the  $c$  axis of  $\text{CaIrO}_3$  shortens less than the  $a$  axis under pressure, it expands much more than the  $a$  axis on heating. In the present work, we have found that  $\text{CaPtO}_3$  also shows behaviour of this type, but that its behaviour differs in

**Table 7**

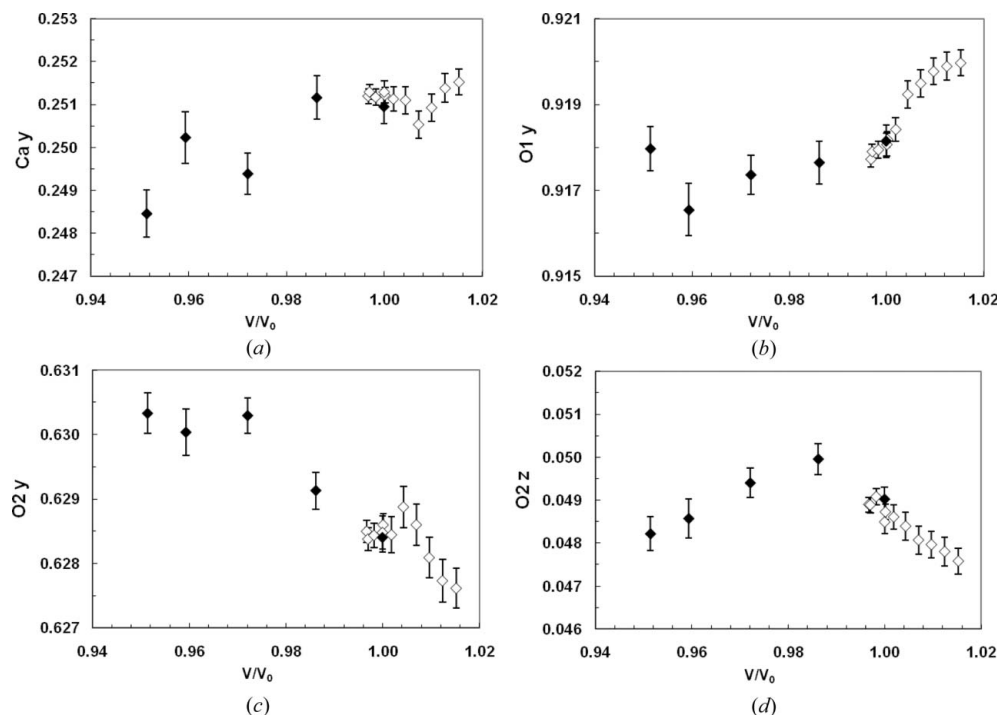
Bond lengths and angles calculated for CaPtO<sub>3</sub> as a function of  $V/V_0$ .

In compression,  $V_0$  was taken to be the equation-of-state value shown in Table 2. On cooling or heating,  $V_0$  was taken to be the measured value at 291 K. The numbers in parentheses are estimated standard uncertainties and refer to the least-significant digits.

$V/V_0$	Pressure (GPa)	Pt—O1 (Å)	Pt—O2 (Å)	Ca—O1 (Å)	Ca—O2 (Å)	Ca—O2' (Å)	$\Delta_1$ (°)	$\Delta_2$ (°)	$p$ (°)	$V_{\text{poly}}$ (Å <sup>3</sup> )	$V_{\text{oct}}$ (Å <sup>3</sup> )	$V_{\text{void}}$ (Å <sup>3</sup> )
0.9514	9.27 (7)	1.987 (5)	2.022 (5)	2.243 (5)	2.416 (5)	2.464 (4)	24.03 (16)	15.51 (13)	99.34 (27)	23.535 (56)	10.565 (14)	20.964 (45)
0.9593	7.69 (9)	1.988 (6)	2.030 (5)	2.243 (6)	2.428 (5)	2.463 (5)	23.85 (19)	15.57 (15)	99.16 (31)	23.744 (64)	10.669 (17)	20.696 (57)
0.9721	5.07 (7)	1.995 (5)	2.033 (4)	2.262 (5)	2.436 (4)	2.488 (4)	23.84 (14)	15.92 (11)	99.43 (24)	24.203 (51)	10.741 (13)	20.460 (53)
0.9862	2.38 (7)	2.001 (5)	2.040 (4)	2.266 (5)	2.457 (5)	2.497 (4)	23.78 (16)	16.13 (12)	99.54 (25)	24.663 (56)	10.848 (14)	20.264 (67)
0.9999	0.02 (5)	2.008 (4)	2.046 (3)	2.281 (4)	2.472 (4)	2.504 (3)	23.76 (12)	15.84 (9)	99.63 (19)	25.082 (44)	10.946 (11)	20.124 (57)

$V/V_0$	Temperature (K)	Pt—O1 (Å)	Pt—O2 (Å)	Ca—O1 (Å)	Ca—O2 (Å)	Ca—O2' (Å)	$\Delta_1$ (°)	$\Delta_2$ (°)	$p$ (°)	$V_{\text{poly}}$ (Å <sup>3</sup> )	$V_{\text{oct}}$ (Å <sup>3</sup> )	$V_{\text{void}}$ (Å <sup>3</sup> )
Cryostat												
0.9967	2	2.008 (2)	2.047 (2)	2.272 (2)	2.469 (2)	2.497 (1)	23.95 (6)	15.75 (4)	99.48 (9)	24.898 (19)	10.949 (5)	20.946 (20)
0.9967	33	2.007 (2)	2.046 (2)	2.271 (2)	2.471 (2)	2.495 (2)	23.88 (5)	15.73 (5)	99.52 (12)	24.924 (24)	10.938 (6)	20.932 (25)
0.9968	66	2.007 (2)	2.047 (2)	2.272 (2)	2.470 (2)	2.496 (2)	23.87 (5)	15.78 (4)	99.48 (10)	24.921 (20)	10.945 (5)	20.932 (21)
0.9970	100	2.008 (2)	2.046 (2)	2.273 (2)	2.470 (2)	2.497 (2)	23.90 (5)	15.76 (4)	99.53 (10)	24.930 (20)	10.940 (5)	20.938 (20)
0.9973	133	2.008 (2)	2.046 (2)	2.272 (2)	2.471 (2)	2.498 (2)	23.90 (5)	15.80 (4)	99.51 (10)	24.935 (20)	10.947 (5)	20.944 (21)
0.9975	150	2.008 (2)	2.047 (2)	2.271 (2)	2.472 (2)	2.496 (1)	23.90 (5)	15.75 (4)	99.50 (9)	24.937 (19)	10.950 (5)	20.951 (20)
0.9977	166	2.009 (2)	2.046 (2)	2.273 (2)	2.470 (2)	2.499 (2)	23.94 (5)	15.79 (4)	99.53 (10)	24.942 (20)	10.950 (5)	20.958 (21)
0.9982	200	2.008 (2)	2.047 (2)	2.275 (2)	2.470 (2)	2.500 (2)	23.89 (5)	15.81 (4)	99.48 (10)	24.954 (22)	10.962 (5)	20.963 (22)
0.9988	233	2.010 (2)	2.047 (2)	2.270 (2)	2.472 (2)	2.500 (2)	23.96 (5)	15.86 (4)	99.50 (10)	24.958 (22)	10.970 (5)	20.983 (23)
0.9994	266	2.009 (2)	2.048 (2)	2.277 (2)	2.469 (2)	2.503 (2)	23.90 (5)	15.84 (4)	99.48 (10)	24.985 (21)	10.975 (5)	20.987 (22)
1.0001	300	2.009 (2)	2.049 (2)	2.277 (2)	2.472 (2)	2.499 (2)	23.83 (5)	15.68 (4)	99.44 (9)	25.001 (20)	10.983 (5)	21.003 (20)
Furnace												
1.0000	291	2.009 (2)	2.048 (2)	2.276 (2)	2.474 (2)	2.497 (2)	23.86 (7)	15.63 (6)	99.50 (13)	25.009 (28)	10.968 (7)	21.002 (29)
1.0019	373	2.009 (2)	2.049 (2)	2.281 (3)	2.474 (3)	2.500 (2)	23.77 (7)	15.67 (6)	99.50 (14)	25.079 (30)	10.984 (7)	21.023 (31)
1.0043	473	2.008 (3)	2.053 (3)	2.289 (3)	2.475 (3)	2.500 (3)	23.55 (9)	15.55 (7)	99.34 (16)	25.142 (34)	11.026 (8)	21.059 (35)
1.0070	573	2.009 (3)	2.053 (3)	2.297 (3)	2.477 (3)	2.504 (3)	23.48 (9)	15.49 (7)	99.47 (16)	25.263 (34)	11.022 (8)	21.093 (35)
1.0097	673	2.010 (3)	2.051 (3)	2.298 (3)	2.484 (3)	2.506 (3)	23.40 (8)	15.52 (7)	99.68 (16)	25.411 (33)	11.006 (8)	21.113 (34)
1.0124	773	2.011 (3)	2.050 (3)	2.297 (3)	2.491 (3)	2.507 (3)	23.37 (9)	15.51 (7)	99.83 (16)	25.534 (35)	11.003 (9)	21.150 (36)
1.0152	869	2.013 (3)	2.051 (2)	2.299 (3)	2.496 (3)	2.508 (3)	23.35 (9)	15.46 (7)	99.89 (15)	25.628 (33)	11.018 (8)	21.202 (33)



**Figure 7**

CaPtO<sub>3</sub> fractional atomic coordinates. (a) Ca  $y$ , (b) O1  $y$ , (c) O2  $y$  and (d) O2  $z$ . Solid symbols are data from compression at 291 K and open symbols are data from cooling or heating at ambient pressure. To improve legibility, only selected data points from the sample in the cryostat (2, 100, 200 and 300 K) have been plotted.

detail from that of CaIrO<sub>3</sub>. For example, in CaPtO<sub>3</sub>, although the  $b$  axis shortens most under pressure it does not expand most on heating. This point is discussed further in §5 below.

### 4.3. Crystal structure refinements of PPV-CaPtO<sub>3</sub>

The fractional atomic coordinates and isotropic displacement parameters for PPV-CaPtO<sub>3</sub> obtained from the Rietveld refinements at high pressure (at 291 K) are given in Table 1; the corresponding values for the measurements made as a function of temperature (at ambient pressure) are given in Table 6. The agreement with the two published structures of CaPtO<sub>3</sub> determined at room temperature from X-ray powder diffraction (Ohgushi *et al.*, 2008; Inaguma *et al.*, 2008) is

reasonably good, bearing in mind the difficulty of determining accurate oxygen coordinates in the presence of platinum by X-ray diffraction. To enable ready comparison of the behaviour of the material as either  $P$  or  $T$  is varied, Fig. 7 shows the fractional coordinates both on compression (solid symbols) and on cooling/heating (open symbols), plotted as a function of  $V/V_0$ , where  $V_0$  is taken to be the unit-cell volume at  $T = 291$  K and  $P = 0$  (strictly, 0.1 MPa). Data collected either in the cryostat below 291 K or on compression have  $V/V_0 < 1$ ;

points for which  $V/V_0 > 1$  correspond to the ambient-pressure isobar above 291 K. Note that, to improve legibility in Figs. 7–10, only selected data points from the sample in the cryostat at 2, 100, 200 and 300 K have been plotted. The fractional coordinates from all three experiments (*i.e.* pressure cell, cryostat and furnace) show good agreement for  $V/V_0 = 1$ , with the measured values at 291 K consistent within one estimated standard uncertainty between the compression, cryostat and furnace experiments. Thus, although the changes in the fractional

atomic coordinates are very small ( $<0.0035$  in all cases), the systematic trends that can be observed in Fig. 7 are probably meaningful.

As described in the introduction, the PPV- $\text{CaPtO}_3$  structure may be defined in terms of the four bond lengths Pt–O1, Pt–O2, Ca–O1 and Ca–O2, and the three angles  $\Delta_1$ ,  $\Delta_2$  and  $p$  required to define the geometry of the  $\text{PtO}_6$  octahedron and its orientation within the unit cell.

The values of these four cation–anion distances for both the 291 K isotherm and the ambient-pressure isobar are listed in Table 7 and shown in Fig. 8; a fifth Ca–O bond length (Ca–O2'), corresponding to the distance between the Ca ion and the O ions that cap the prism faces of the  $\text{CaO}_8$  coordination polyhedron, is included for completeness. Since only the Bragg reflections have been considered in the data analysis, the bond distances discussed here correspond to the interatomic separations in the average crystal structure, uncorrected for thermal motion. The angles  $\Delta_1$ ,  $\Delta_2$  and  $p$  are also listed in Table 7 and are shown in Fig. 9. Fig. 10 shows the changes in the volumes of the  $\text{CaO}_8$  coordination hendecahedron, the  $\text{PtO}_6$  octahedron and the void space in the unit cell not occupied by hendecahedra or octahedra (numerical values are listed in Table 7). Finally, the seven shortest O–O distances are shown in Fig. 11.

The isotropic displacement parameters from the Rietveld refinements, listed in Tables 1

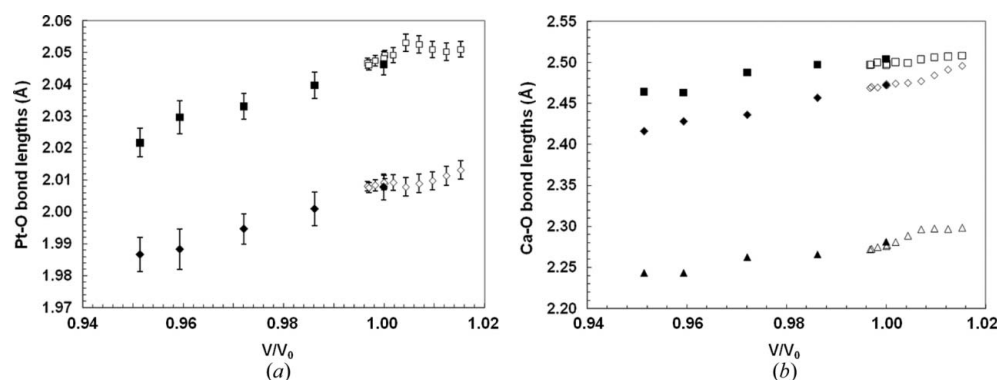


**Figure 8**  $\text{CaPtO}_3$  bond lengths. (a) Pt–O bonds. Diamonds represent data for Pt–O1 and squares Pt–O2. (b) Ca–O bonds. Triangles represent data for Ca–O1, diamonds Ca–O2 and squares Ca–O2'. Estimated uncertainties in the Ca–O bond distances are the same size as the symbols, due to the larger vertical scale. Solid symbols are for data obtained on compression and open symbols are for data from cooling or heating at ambient pressure. To improve legibility, only selected data points from the sample in the cryostat (2, 100, 200 and 300 K) have been plotted.

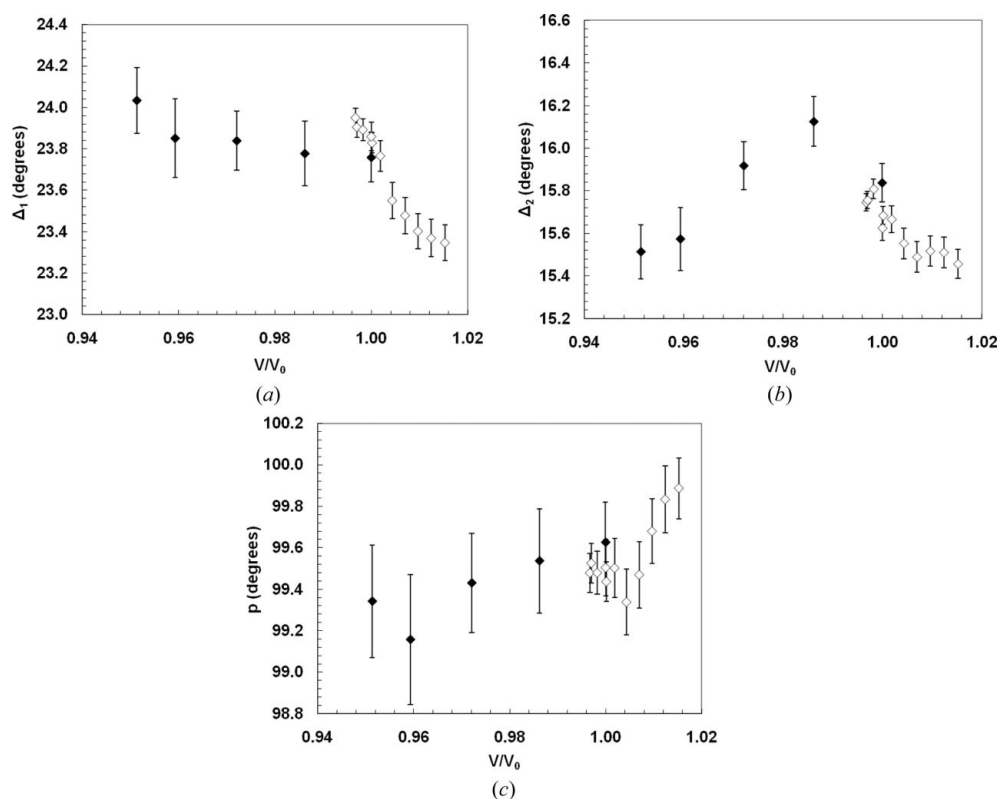


**Figure 9**  $\text{CaPtO}_3$  angles. (a)  $\Delta_1$ , (b)  $\Delta_2$  and (c)  $p$ . Solid symbols are for data obtained on compression and open symbols are for data from cooling or heating at ambient pressure. To improve legibility, only selected data points from the sample in the cryostat (2, 100, 200 and 300 K) have been plotted.

**Table 8**

Anisotropic atomic displacement parameters for  $\text{CaPtO}_3$  at 869 K ( $\text{\AA}^2 \times 100$ ).

The numbers in parentheses are estimated standard uncertainties and refer to the least-significant digits.

Atom	$U_{11}$	$U_{22}$	$U_{33}$	$U_{23}$
Ca	1.74 (16)	1.12 (17)	2.43 (17)	
Pt	0.91 (8)	0.69 (9)	0.72 (7)	0.03 (5)
O1	2.28 (14)	0.85 (12)	1.06 (13)	
O2	1.78 (10)	0.45 (10)	1.22 (9)	-0.19 (6)

and 6, show the expected form, increasing with temperature and decreasing slightly with pressure. In general, they take the form  $U_{\text{Pt}} < U_{\text{O1}} \approx U_{\text{O2}} < U_{\text{Ca}}$ . However, the refined values are sensitive both to the absorption correction applied to the data and to the preferred orientation correction, showing a marked

increase ( $\sim 0.002 \text{ \AA}^2$ ) at room temperature between the values determined with the sample in the cryostat and in the furnace. For this reason, we have not attempted to interpret them in terms of the vibrational frequencies of the atoms as we have done previously for perovskites (*e.g.* Wood *et al.*, 2002).

Although we did not consider our data to be sufficiently good to allow anisotropic atomic displacements to be used in general, we did refine the data sets collected at the three highest useable temperatures (673 K and above) against such a model. The resulting displacement parameters from the refinement at 869 K are shown in Table 8 (note also that the average  $U_{ij}$  values from the three anisotropic refinements at 673, 773 and 869 K are quite similar in form to those shown in this table). Although the site symmetry of all four atoms allows the atomic probability density to take the form of triaxial ellipsoids, it also requires that, for Ca and O1, the

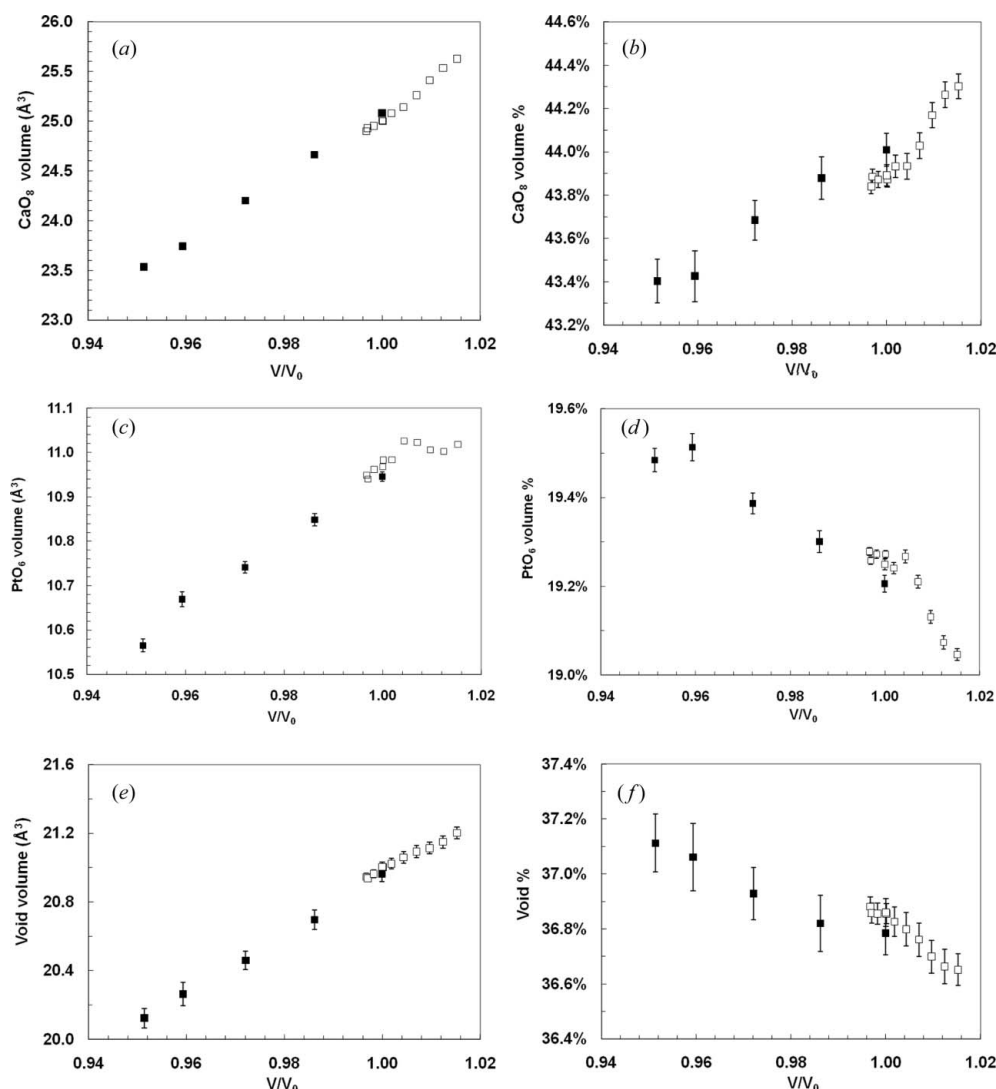


**Figure 10**

$\text{CaPtO}_3$  volumes. (a)  $\text{CaO}_8$  hendecahedron. (b)  $\text{CaO}_8$  hendecahedron volume as a percentage of unit-cell volume. (c)  $\text{PtO}_6$  octahedron. (d)  $\text{PtO}_6$  octahedron volume as a percentage of unit-cell volume. (e) Void volume. (f) Void volume as a percentage of unit-cell volume. Solid symbols are for data obtained on compression and open symbols are for data from cooling or heating at ambient pressure. To improve legibility, only selected data points from the sample in the cryostat (2, 100, 200 and 300 K) have been plotted. Where they are not indicated, estimated standard uncertainties are smaller than the symbols.

principal axes of these ellipsoids must lie parallel to the unit-cell axes. For Pt and O2, the ellipsoids are allowed one degree of rotational freedom, about a line parallel to [100]. It is interesting to note that the probability ellipsoid of the O1 (apical) ion is a prolate spheroid, with the largest component of vibration along [100], which would correspond to a buckling of the rods of  $\text{PtO}_6$  octahedra about the shared-edge ‘hinges’. In contrast, the ellipsoids corresponding to the Ca and O2 ions are oblate spheroids, with their smallest components parallel or nearly parallel (inclined at  $13^\circ$ ) to the  $b$  axis of the unit cell. As might be expected, the ellipsoid of the Pt atom is the smallest in magnitude and the most isotropic. There are currently no published single-crystal measurements of the anisotropic displacement parameters of any oxide post-perovskite at high temperature. Two previous single-crystal X-ray diffraction studies of  $\text{PPV-CaIrO}_3$  have been reported but only at room temperature. Sugahara *et al.* (2008) found a high degree of anisotropy in the atomic displacements, a result which was disputed by Hirai *et al.* (2009), who suggested that it was possibly an artefact resulting from an inadequate absorption correction (the absorption coef-

ficient of  $\text{CaIrO}_3$ , even for Mo radiation, is very high, at  $\sim 61 \text{ mm}^{-1}$ ). At room temperature, Hirai *et al.* (2009) found that there was no significant anisotropy in the atomic displacement parameters of any atoms. However, they also concluded that, despite their higher mass, the magnitudes of the displacement parameters for the Ca ions were of the same magnitude as those of the O ions, an observation which is in agreement with the results shown in Table 8.

## 5. Discussion

### 5.1. The pressure and temperature dependence of the unit-cell parameters of the PPV phases of $\text{CaPtO}_3$ , $\text{CaIrO}_3$ and $\text{MgSiO}_3$

If a PPV material is to be a ‘successful’ analogue of  $\text{PPV-MgSiO}_3$ , it is expected that its cell parameters will respond to changes in pressure and temperature (with respect to ambient  $P$  and  $T$ ) in a similar way to those of  $\text{PPV-MgSiO}_3$  (with respect to lower-mantle values of  $P$  and  $T$ ). However, we have found that, although the anisotropy of axial compression of  $\text{PPV-CaPtO}_3$  (and  $\text{PPV-CaIrO}_3$ ) is similar to that of  $\text{PPV-MgSiO}_3$ , the anisotropy of axial thermal expansion in  $\text{PPV-CaPtO}_3$  differs both from that of  $\text{PPV-MgSiO}_3$  and from that of  $\text{PPV-CaIrO}_3$ . Axial compression and expansion can be compared for  $\text{MgSiO}_3$ ,  $\text{CaPtO}_3$  and  $\text{CaIrO}_3$  (and also with the bulk properties of the materials) by plotting the cubes of the axial compression and expansion ratios ( $i/i_0$ )<sup>3</sup> (where  $i$  is the  $a$ ,

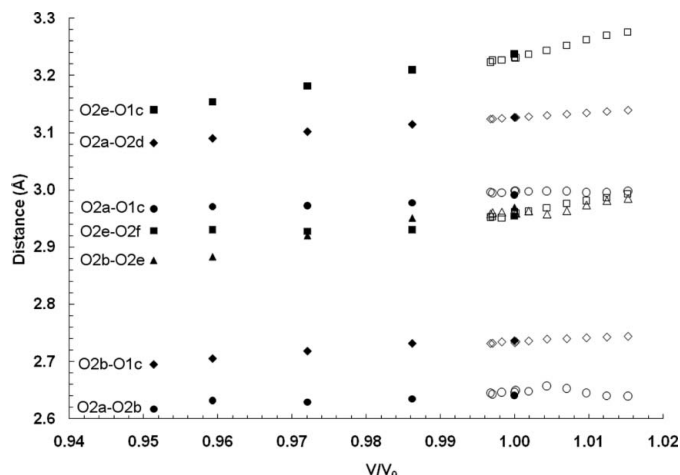


**Figure 11**

O—O distances in  $\text{CaPtO}_3$ . Solid symbols are for data obtained on compression and open symbols are for data from cooling or heating at ambient pressure. To improve legibility, only selected data points from the sample in the cryostat (2, 100, 200 and 300 K) have been plotted. See Figs. 1(a) and 1(c) for the key to the oxygen anion positions.  $\text{O2a-O2b}$  and  $\text{O2a-O2d}$  form the shorter and longer sides of the central plane of the octahedron, respectively.  $\text{O2b-O1c}$  and  $\text{O2a-O1c}$  form the shorter and longer distances from the central plane O2 anions to the apical anion.  $\text{O2a-O2d}$  (equal to the cell parameter  $a$ ) is the length of the trigonal-prism component of the  $\text{CaO}_6$  hendecahedron along [100].  $\text{O2e-O1c}$  is the length of the two equal sides of the isosceles triangle defining the trigonal-prism component of the hendecahedron, and  $\text{O2e-O2f}$  is the length of its base.  $\text{O2b-O1c}$  forms the shorter of the two sides of the hendecahedral prism cap and  $\text{O2b-O2e}$  is the longer of the two sides of the prism cap. Estimated standard uncertainties are smaller than the symbols.

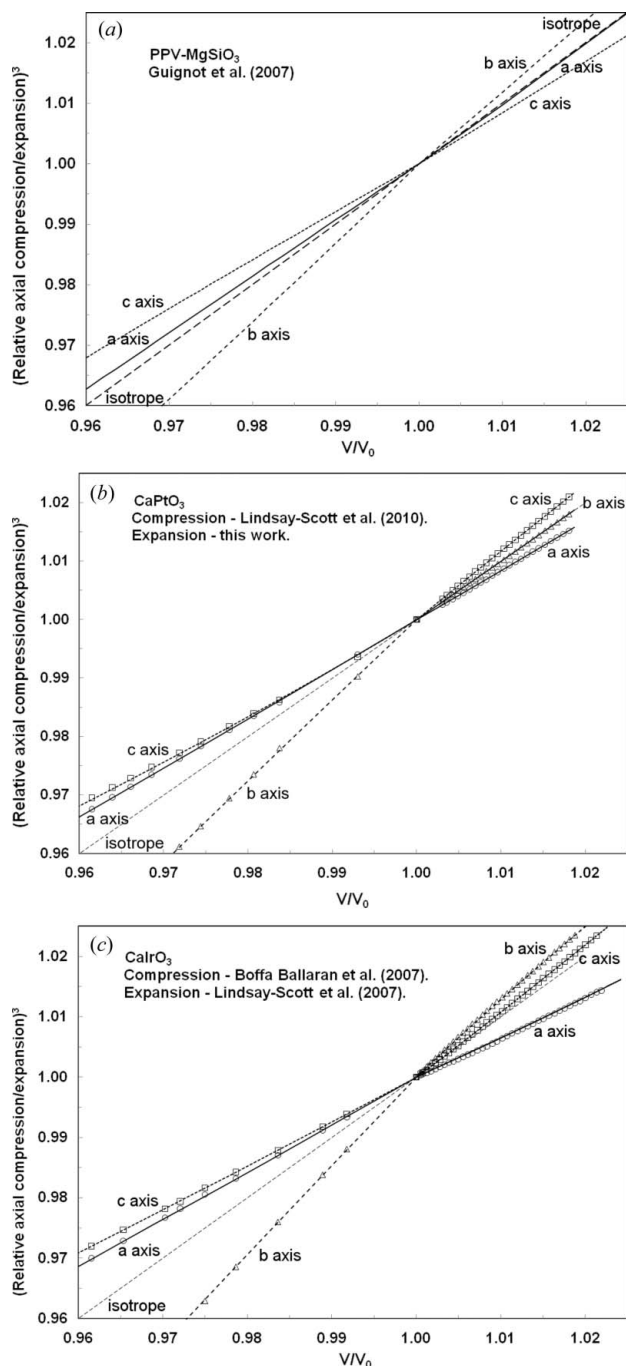


**Figure 12**

Axial expansion and compression of (a)  $\text{MgSiO}_3$  [from Guignot *et al.* (2007)], (b)  $\text{CaPtO}_3$  [compression data from Lindsay-Scott *et al.* (2010); expansion data from the present work] and (c)  $\text{CaIrO}_3$  [compression data from Boffa Ballaran *et al.* (2007); expansion data from Lindsay-Scott *et al.* (2007)], shown as the ratios  $(i/i_0)^3$  (where  $i$  is the  $a$ ,  $b$  or  $c$  unit-cell parameter). Experimental values are shown as points in (b) and (c), with lines showing their fit to third-order Birch–Murnaghan equations of state (compression) or to thermal expansion models. The lines shown in (a) indicate mean values derived from equations of state. The isotrope where  $(i/i_0)^3 = (V/V_0)$  is shown as a dashed line. A  $V_0$  value of 1.0 in (b) and (c) corresponds to ambient temperature and pressure. A  $V_0$  value of 1.0 in (a) corresponds to 137.3 GPa and 2535 K (Guignot *et al.*, 2007). Points for which  $V/V_0 < 1$  correspond to compression of the material. Points for which  $V/V_0 > 1$  correspond to thermal expansion on heating. In (b) and (c), error bars on the experimental values are smaller than the symbols used. Note also that the results of Martin, Chapman *et al.* (2007) for  $\text{PPV-CaIrO}_3$  are very similar to those shown in (c).

*b* or *c* unit-cell parameter) against  $V/V_0$ . Fig. 12(a) shows such a plot for PPV-MgSiO<sub>3</sub> at high pressure and temperature, obtained using equations of state derived from experiment (Guignot *et al.*, 2007). It can be seen that, in MgSiO<sub>3</sub>, the axial compression sequence  $\kappa_c > \kappa_a > \kappa_b$  is the reverse of the expansion sequence  $\alpha_b > \alpha_a > \alpha_c$ . For PPV-CaPtO<sub>3</sub> (Fig. 12b), the behaviour on compression is quite similar to that of PPV-MgSiO<sub>3</sub>, though CaPtO<sub>3</sub> shows greater anisotropy. However, although PPV-CaPtO<sub>3</sub> has the same axial compression sequence,  $\kappa_c > \kappa_a > \kappa_b$ , as PPV-MgSiO<sub>3</sub>, it shows a different thermal expansion sequence, with  $\alpha_c > \alpha_b > \alpha_a$ . Thus, the *b* axis in CaPtO<sub>3</sub> expands much less when heated than might naively be expected from its change in length on compression, and the *c* axis expands more. CaIrO<sub>3</sub> (Fig. 12c) has the same axial compression sequence as both MgSiO<sub>3</sub> and CaPtO<sub>3</sub> (though with a slightly greater anisotropy than CaPtO<sub>3</sub>), but on expansion the sequence  $\alpha_b > \alpha_c > \alpha_a$  is observed. Bearing in mind their similar behaviour under pressure, this difference in the properties of CaIrO<sub>3</sub> and CaPtO<sub>3</sub> on heating is very striking; not only is the order of expansion of their *b* and *c* axes reversed, but CaIrO<sub>3</sub> also shows much greater anisotropy.

## 5.2. The pressure and temperature dependence of the crystal structure of PPV-CaPtO<sub>3</sub>

Fig. 7 shows the variation in the atomic coordinates (listed in Tables 1 and 6) of PPV-CaPtO<sub>3</sub> with  $V/V_0$ . If the values on the ambient-*P* isobar below 291 K are discounted, it can be seen that O1 *y* is the only atomic coordinate to show a monotonic change across the full range of  $V/V_0$ , *i.e.* as the material passes from the regime of compression to that of thermal expansion. Ca *y* shows a local minimum at 573 K, O2 *y* a local maximum at 473 K and O2 *z* a global maximum at 2.38 GPa. However, the changes in the structure are very small, and thus the local minima and maxima in Ca *y* and O2 *y* may not be significant, although the trends appear to be systematic. These characteristics are reflected in the inter-atomic distances and geometric parameters derived from the coordinates (as determined from the average positions of the atoms in the crystal structure, uncorrected for thermal motion). Thus, the O2 *y* local maximum is associated with both the maximum in the Pt–O2 bond length (Fig. 8a) and the local minimum in the angle *p* at 473 K (Fig. 9c). Similarly, the maximum in O2 *z* corresponds to the maximum in the  $\Delta_2$  tilt angle at 2.38 GPa (Fig. 9b).

All Ca–O and Pt–O bond lengths are observed to decrease on compression (Fig. 8). However, the behaviour on heating is less simple, with the Pt–O2 bond distance reaching a maximum at 473 K, after which it appears to saturate, or possibly to decline slowly. Similarly, there appears to be a plateau in the Ca–O1 bond length above 573 K, though this is less obvious (Fig. 8). The behaviour of the average structure of CaPtO<sub>3</sub> thus differs from that reported for CaIrO<sub>3</sub> by Martin, Chapman *et al.* (2007), in which the Ir–O2 and Ca–O1 distances [as calculated from the equations given in Fig. 4 of Martin, Chapman *et al.* (2007)] were found to shorten on heating. The  $\Delta_1$  tilt of the octahedron changes little on

compression but decreases on heating (Fig. 9a). The  $\Delta_2$  tilt decreases from its maximum near 2.38 GPa, both when compressed and when heated (Fig. 9b). The angle *p* decreases with compression and increases with heating (Fig. 9c), since under pressure the shorter O2a–O2b bond is stiffer than the O2a–O2d bond (Fig. 11), whilst on heating above 473 K, O2a–O2d increases steadily but O2a–O2b decreases.

The volumes of both the PtO<sub>6</sub> octahedron and the CaO<sub>8</sub> hendecahedron decrease under compression and increase on heating (Fig. 10), although the octahedral volume appears to saturate above 473 K, possibly decreasing slightly thereafter. This effect arises from the insignificant expansion of the octahedral O1–O2 distances above room temperature (Fig. 11), combined with a shortening of the Pt–O2 distance by a decrease in O2 *y* and O2 *z* (Figs. 7c and 7d). However, consideration of the proportion of the unit-cell volume occupied by the two different coordination polyhedra and the void space reveals a difference in behaviour. The percentage volumes occupied by the octahedra (Fig. 10d) and by the void space (Fig. 10f) fall with increasing  $V/V_0$ , whereas the proportion occupied by the hendecahedra (Fig. 10b) rises.

## 5.3. The relationship between the crystal structure and unit-cell parameters of CaPtO<sub>3</sub>

In order to determine the physical origin of the difference in behaviour of the unit-cell parameters of CaPtO<sub>3</sub> shown on compression and on heating, it is instructive to analyse the axial compression and expansion in terms of equations (4)–(6) (*i.e.* in terms of the four shortest cation–anion bond distances in the structure, and the three angles,  $\Delta_1$ ,  $\Delta_2$  and *p*, needed to specify the geometry and linkage of the PtO<sub>6</sub> octahedron). Since the changes in magnitude of all of the quantities are small, from equation (4), for example, we may write

$$da = \left[ \frac{\partial a}{\partial(\text{Pt} - \text{O}2)} \right]_p d(\text{Pt} - \text{O}2) + \left( \frac{\partial a}{\partial p} \right)_{(\text{Pt} - \text{O}2)} dp, \quad (13)$$

where

$$\left[ \frac{\partial a}{\partial(\text{Pt} - \text{O}2)} \right]_p = 2 \sin(p/2) \quad (14)$$

and

$$\left( \frac{\partial a}{\partial p} \right)_{(\text{Pt} - \text{O}2)} = (\text{Pt} - \text{O}2) \cos(p/2). \quad (15)$$

Similar equations can be obtained for the *b* and *c* axes (for convenience, the seven partial derivatives required for the analysis of the *b* axis were calculated numerically).

Table 9(a) shows the relative importance of each of the contributing factors to the change in length of the unit-cell axes of CaPtO<sub>3</sub>, during both compression (results are compared from the data collected at 0.02 and 9.27 GPa) and expansion (results from data collected at 291 and 869 K). It can be seen that, despite the fact that different bonds and angles are involved, the *a* and *c* axes show remarkable similarity in behaviour. For both the *a* and *c* axes, the dominant compression mechanism is by a shortening of the Pt–O

bonds, this term accounting for ~85% of the observed shortening, with only 15% coming from changes in the angle  $p$  specifying the geometry of the central plane of the octahedron (for the  $a$  axis) or the angle  $\Delta_1$  specifying the orientation of the apical O atoms of the octahedron (for the  $c$  axis). On heating, however, the mechanism for expansion is clearly very different, as now 66% of the increase in length results from changes in angles and only 34% from expansion of the Pt–O bonds. Understanding the origin of the behaviour observed for the  $b$  axis is a little more complex, as the length of this axis depends on all four of the bond lengths and all three angles, but some general conclusions may still be drawn. Under pressure, shortening of the  $b$  axis results largely from shortening of the Ca–O bonds, especially the Ca–O2 bond; the changes in the Pt–O bonds and the three angles ( $\Delta_1$ ,  $\Delta_2$  and  $p$ ), taken individually, each produce only a small effect. On heating, the expansion of the  $b$  axis arises from expansion of the Ca–O bonds, but the angles  $p$  and  $\Delta_1$  now both provide a major contribution, acting in the opposite sense to the change in Ca–O bond lengths. It is interesting to note that lengthening of either of the Pt–O bonds or increasing the angle  $p$  (other quantities remaining constant) produces a shortening of the  $b$  axis. In the case of Pt–O2 and  $p$ , this arises because the increase in the length of the  $a$  axis that arises from an increase in either Pt–O2 or  $p$  must produce a decrease in the length of the  $b$  axis if the Ca–O2 distance is to remain constant. A similar argument applies for Pt–O1; an increase in the length of this bond increases the length of the  $c$  axis, which in turn (for a constant Ca–O2 distance) must result in the  $b$  axis becoming smaller.

#### 5.4. Comparison with PPV-CaIrO<sub>3</sub> and PPV-MgSiO<sub>3</sub>

The approach described above for determining the mechanisms of the changes in cell parameters under pressure and on heating may also be used to examine the difference in behaviour between CaPtO<sub>3</sub>, CaIrO<sub>3</sub> and MgSiO<sub>3</sub>.

The change in the average structure of PPV-CaIrO<sub>3</sub> under compression has been studied by Rietveld refinement to 10 GPa using neutron powder diffraction by Martin, Smith *et al.* (2007), and on heating to 1109 K by X-ray powder diffraction by Martin, Chapman *et al.* (2007). Table 9(b) shows the contributions from the different elements of the crystal structure to the changes in length of the unit-cell axes. On compression, this structure appears to respond in quite a similar way to that of CaPtO<sub>3</sub>, with the change in length of the axes produced mainly by a

**Table 9**

Relative importance (%) of changes in bond distances and angles in determining the change in unit-cell parameters during compression and expansion.

Note that, in compression, a positive contribution is taken as one that shortens the axis as the applied pressure is increased, whereas for expansion a positive contribution corresponds to a lengthening of the axis as the temperature is raised. The calculated changes in the lengths of the axes produced by the approximation that they depend linearly on the changes in the four bond distances and three angles ( $p$ ,  $\Delta_1$  and  $\Delta_2$ ) are always within 1% of their observed values for CaPtO<sub>3</sub>, 5% of their observed values for CaIrO<sub>3</sub> and 3% of their observed values for MgSiO<sub>3</sub>.

(a) CaPtO<sub>3</sub> (present work).

Compression: 0.02 GPa versus 9.265 GPa ( $V/V_0 = 0.951$ ).

Expansion: 291 K versus 869 K ( $V/V_0 = 1.015$ ).

*a* axis

	Percentage of calculated change in <i>a</i> due to change in Pt–O2 bond	Percentage of calculated change in <i>a</i> due to change in angle $p$
Compression	85	15
Expansion	34	66

*b* axis

	Percentage of calculated change in <i>b</i> due to change in						
	Pt–O1 bond	Pt–O2 bond	Ca–O1 bond	Ca–O2 bond	Angle $p$	Angle $\Delta_1$	Angle $\Delta_2$
Compression	–13	–19	47	101	–11	–12	6
Expansion	–11	–10	125	177	–66	–101	–14

*c* axis

	Percentage of calculated change in <i>c</i> due to change in Pt–O1 bond	Percentage of calculated change in <i>c</i> due to change in angle $\Delta_1$
Compression	83	17
Expansion	33	67

(b) CaIrO<sub>3</sub>. Table calculated using crystal structures taken from the following:

Compression: 0.0 GPa versus 9.72 GPa ( $V/V_0 = 0.952$ ); Martin, Smith *et al.* (2007).

Expansion: 332 K versus 1109 K ( $V/V_0 = 1.026$ ); Martin, Chapman *et al.* (2007).

*a* axis

	Percentage of calculated change in <i>a</i> due to change in Ir–O2 bond	Percentage of calculated change in <i>a</i> due to change in angle $p$
Compression	59	41
Expansion	–131	231

*b* axis

	Percentage of calculated change in <i>b</i> due to change in						
	Ir–O1 bond	Ir–O2 bond	Ca–O1 bond	Ca–O2 bond	Angle $p$	Angle $\Delta_1$	Angle $\Delta_2$
Compression	–13	–13	49	121	–29	–16	0
Expansion	–52	24	–65	218	–144	116	0

*c* axis

	Percentage of calculated change in <i>c</i> due to change in Ir–O1 bond	Percentage of calculated change in <i>c</i> due to change in angle $\Delta_1$
Compression	78	22
Expansion	193	–93

(c) MgSiO<sub>3</sub>. Table calculated using crystal structures taken from the following:

Compression: 136 GPa *versus* 178 GPa ( $V/V_0 = 0.946$ ); athermal *ab initio* computer simulations using the *VASP* program (Lindsay-Scott, unpublished).

Expansion: 500 K *versus* 4000 K ( $V/V_0 = 1.043$ ) at 136 GPa; *ab initio* quantum molecular dynamics computer simulations using the *VASP* program (Stackhouse & Brodholt, 2007).

*a* axis

	Percentage of calculated change in <i>a</i> due to change in Si—O2 bond	Percentage of calculated change in <i>a</i> due to change in angle <i>p</i>
Compression	87	13
Expansion	102	-2

*b* axis

	Percentage of calculated change in <i>b</i> due to change in						
	Si—O1 bond	Si—O2 bond	Mg—O1 bond	Mg—O2 bond	Angle <i>p</i>	Angle Δ <sub>1</sub>	Angle Δ <sub>2</sub>
Compression	-24	-18	50	96	-9	10	-1
Expansion	-23	-27	66	96	2	-13	-1

*c* axis

	Percentage of calculated change in <i>c</i> due to change in Si—O1 bond	Percentage of calculated change in <i>c</i> due to change in angle Δ <sub>1</sub>
Compression	109	-9
Expansion	89	11

decrease in the Ir—O distances (for *a* and *c*) and a decrease in the Ca—O distances (for *b*). However, it appears that changes in the angles Δ<sub>1</sub>, Δ<sub>2</sub> and *p* may play a somewhat larger role in this material, especially in the case of the *a* axis. On heating, the behaviour shown by CaIrO<sub>3</sub> appears to be completely different from that of CaPtO<sub>3</sub>, with, for example, a contraction of the Ir—O2 bond producing a shortening of the *a* axis which is then overcome by an increase in the angle *p*. However, because of the dominance of the scattering from the Ir atoms, the oxygen coordinates in the high-temperature structures of CaIrO<sub>3</sub> are very difficult to determine accurately by X-ray powder diffraction and so we believe that these results should be treated with caution. Martin, Chapman *et al.* (2007) found that both the Ca—O1 and Ir—O2 bond lengths in the average structure of CaIrO<sub>3</sub> showed significant negative thermal expansion and that the IrO<sub>6</sub> octahedra decreased in volume with increasing temperature (somewhat similar to the plateau in the Ca—O1 bond length above 573 K and the shrinkage in the Pt—O2 bond length and PtO<sub>6</sub> octahedral volume between 473 and 773 K found in the present study). A subsequent examination of X-ray powder data from CaIrO<sub>3</sub> at high temperature using a pair distribution function approach (Martin, 2008) suggested that the apparent decrease in the length of these bonds with temperature may be an artefact resulting from the effect of thermal motion on the average positions of the atoms. Such effects would appear to be less significant for CaPtO<sub>3</sub> than for CaIrO<sub>3</sub>. In this connection, it is of interest to note that recent *ab initio* quantum molecular dynamics simulations of CaIrO<sub>3</sub> and CaPtO<sub>3</sub> (Lindsay-Scott, unpublished) produce an Ir—O2 distance computed from the

average positions of the atoms that is almost temperature invariant, although the average of the instantaneous Ir—O2 distances at each simulation step increases; in contrast, the corresponding values for Pt—O2 both show a clear increase with temperature.

The crystal structure of PPV-MgSiO<sub>3</sub> has been studied as a function of pressure by Shim *et al.* (2008), but the relatively large uncertainties in the atomic coordinates from this high-pressure X-ray diffraction DAC study make a detailed comparison of the structural changes on compression very difficult. However, the reported decrease in the angle *p* with increasing pressure is consistent with the results of the present study. Since accurate crystal structure determinations of MgSiO<sub>3</sub> are not available as a function of either *P* or *T*, Table 9(c) shows, instead, an analysis of the relationship between crystal structure and cell-parameter changes in MgSiO<sub>3</sub> based on two sets of computer simulations. To obtain the compression data, athermal *ab initio* simulations were made using the *VASP* computer code (Lindsay-Scott, unpublished); for the expansion data, the *ab initio* molecular dynamics results of Stackhouse & Brodholt (2007) at simultaneous high *P* and high *T* were used. Once again, it would seem that, under pressure, the structure distorts mainly by shortening of the Si—O and Mg—O bond

distances in a similar manner to that shown by CaPtO<sub>3</sub> and CaIrO<sub>3</sub>. On heating, however, it seems that MgSiO<sub>3</sub> behaves differently from the two analogue compounds, with changes in bond length still dominating the expansion mechanism.

### 5.5. PPV-CaPtO<sub>3</sub> and PPV-CaIrO<sub>3</sub> as low-pressure analogues of PPV-MgSiO<sub>3</sub>

PPV-CaPtO<sub>3</sub> and PPV-CaIrO<sub>3</sub> have the same axial compression sequence ( $\kappa_c > \kappa_a > \kappa_b$ ) as PPV-MgSiO<sub>3</sub>, but each of the three compounds has a different axial expansion sequence. If the atomic coordinates from the *ab initio* molecular dynamics simulations of MgSiO<sub>3</sub> are accurate, the analysis presented above would seem to provide a ready explanation for these differences in behaviour. Since the response to pressure shown by CaPtO<sub>3</sub> and CaIrO<sub>3</sub> is similar to that of MgSiO<sub>3</sub>, it might be argued that either compound could provide a suitable low-pressure analogue for MgSiO<sub>3</sub>, with CaPtO<sub>3</sub> being marginally better as it is less anisotropic in compression than CaIrO<sub>3</sub>. However, in the *D''* region of the Earth, within 200–300 km of the core–mantle boundary, where PPV-MgSiO<sub>3</sub> is thought to exist, the range of pressure encountered is quite small, varying from about 118 to 136 GPa (Dziewonski & Anderson, 1981). In contrast, the change in temperature across this region is large, probably more than 1000 K between the top and the bottom of the *D''* region (*e.g.* from ~2600 K to 3700–4100 K; Trønnes, 2010). The *P–V–T* equation of state for PPV-MgSiO<sub>3</sub> determined by Guignot *et al.* (2007) predicts that an isothermal change in pressure (at 2535 K) from 118 to 136 GPa will result in a 3.1% reduction in

volume, whereas isobaric changes in temperature (at 110–150 GPa) from 2600 K to either 3700 or 4100 K will result in volume increases of 1.4 or 2.0%, respectively. Thus, the change in volume of PPV-MgSiO<sub>3</sub> due to the change in temperature across the D'' layer is expected to be similar to that due to the change in pressure and there is no reason to suppose, *a priori*, that significant temperature effects will not be found for the other physical properties of MgSiO<sub>3</sub>. The differences in the axial expansion behaviour shown by CaPtO<sub>3</sub> and CaIrO<sub>3</sub> at 0 GPa from that of MgSiO<sub>3</sub> at high pressure must, therefore, substantially weaken the case for using either of these compounds as low-pressure analogues of MgSiO<sub>3</sub> to aid understanding of the D'' layer.

ALS is funded by a postgraduate studentship from the Natural Environment Research Council. Mr Christopher Barry is thanked for experimental assistance at PEARL, and Dr Dominic Fortes for assistance with the PEARL pressure calibration.

## References

- Angel, R. J. (2000). *Equations of State*, edited by R. M. Hazen & R. T. Downs, Reviews in Mineralogy and Geochemistry, Vol. 41. Washington, DC: Mineralogical Society of America.
- Angel, R. J. (2001). *EOS-FIT*. Version 5.2. Crystallography Laboratory, Department of Geological Sciences, Virginia Tech, Blacksburg, Virginia, USA.
- Bergner, D. & Kohlhaas, R. (1973). *Z. Anorg. Allg. Chem.* **401**, 15–20.
- Birch, F. (1978). *J. Geophys. Res.* **83**, 1257–1268.
- Boffa Ballaran, T., Trønnes, R. G. & Frost, D. J. (2007). *Am. Mineral.* **92**, 1760–1763.
- Bremholm, M., Dutton, S. E., Stephens, P. W. & Cava, R. J. (2011). *J. Solid State Chem.* **184**, 601–607.
- Dziewonski, A. M. & Anderson, D. L. (1981). *Phys. Earth Planet. Inter.* **25**, 297–356.
- Fei, Y. (1995). *AGU Reference Shelf 2: Mineral Physics and Crystallography – A Handbook of Physical Constants*, edited by T. J. Ahrens, pp. 29–44. Washington, DC: American Geophysical Union.
- Fortes, A. D., Wood, I. G., Alfredsson, M., Vočadlo, L., Knight, K. S., Marshall, W. G., Tucker, M. G. & Fernandez-Alonso, F. (2007). *High Press. Res.* **27**, 201–212.
- Fortes, A. D., Wood, I. G. & Knight, K. S. (2006). *J. Chem. Phys.* **125**, 144510.
- Fortes, A. D., Wood, I. G., Vocadlo, L., Chapon, L., Knight, K. S. & Smith, R. I. (2008). *J. Chem. Phys.* **128**, 054506.
- Guignot, N., Andrault, D., Morard, G., Bolfan-Casanova, N. & Mezouar, M. (2007). *Earth Planet. Sci. Lett.* **256**, 162–168.
- Hirai, S., Welch, M. D., Aguado, F. & Redfern, S. A. T. (2009). *Z. Kristallogr.* **224**, 345–350.
- Ibberson, R. M., David, W. I. F. & Knight, K. S. (1992). Report RAL-92-031. Rutherford Appleton Laboratory, Didcot, Oxfordshire, England.
- Inaguma, Y., Hasumi, K., Yoshida, M., Ohba, T. & Katsumata, T. (2008). *Inorg. Chem.* **47**, 1868–1870.
- ISIS Annual Report (1996). Report RAL-TR-96-050, pp. 61–62. Rutherford Appleton Laboratory, Didcot, Oxfordshire, England.
- Kubo, A., Kiefer, B., Shim, S.-H., Shen, G., Prakapenka, V. B. & Duffy, T. S. (2008). *Am. Mineral.* **93**, 965–976.
- Larson, A. C. & Von Dreele, R. B. (1994). *GSAS*. Report LAUR 86-748. Los Alamos National Laboratory, New Mexico, USA.
- Le Bail, A., Duroy, H. & Fourquet, J. L. (1988). *Mater. Res. Bull.* **23**, 447–452.
- Lindsay-Scott, A., Wood, I. G. & Dobson, D. (2007). *Phys. Earth Planet. Inter.* **162**, 140–148.
- Lindsay-Scott, A., Wood, I. G., Dobson, D., Vočadlo, L., Brodholt, J. P., Crichton, W., Hanfland, M. & Taniguchi, T. (2010). *Phys. Earth Planet. Inter.* **182**, 113–118.
- Liu, W., Whitaker, M. L., Liu, Q., Wang, L., Nishiyama, N., Wang, Y., Kubo, A., Duffy, T. S. & Li, B. (2011). *Phys. Chem. Miner.* **38**, 407–417.
- Mantid (2010). *MANTID Project Main Page*, [http://www.mantidproject.org/Main\\_Page](http://www.mantidproject.org/Main_Page).
- Marshall, W. G. & Francis, D. J. (2002). *J. Appl. Cryst.* **35**, 122–125.
- Martin, C. D. (2008). *J. Appl. Cryst.* **41**, 776–783.
- Martin, C. D., Chapman, K. W., Chupas, P. J., Prakapenka, V., Lee, P. L., Shastri, S. D. & Parise, J. B. (2007). *Am. Mineral.* **92**, 1048–1053.
- Martin, C. D., Smith, R. I., Marshall, W. G. & Parise, J. B. (2007). *Am. Mineral.* **92**, 1912–1918.
- Murakami, M., Hirose, K., Kawamura, K., Sata, N. & Ohishi, Y. (2004). *Science*, **304**, 855–858.
- Niwa, K., Yagi, T. & Ohgushi, K. (2011). *Phys. Chem. Miner.* **38**, 21–31.
- Oganov, A. R. & Ono, S. (2004). *Nature (London)*, **430**, 445–448.
- Ohgushi, K., Matsushita, Y., Miyajima, N., Katsuya, Y., Tanaka, M., Izumi, F., Gotou, H., Ueda, Y. & Yagi, T. (2008). *Phys. Chem. Miner.* **35**, 189–195.
- Poirier, J.-P. (2000). *Introduction to the Physics of the Earth's Interior*, 2nd ed. Cambridge University Press.
- Scientific Computing World (2008). *ISIS Gears Up for a Data Deluge*, [http://www.scientific-computing.com/news/news\\_story.php?news\\_id=327](http://www.scientific-computing.com/news/news_story.php?news_id=327).
- Shim, S.-H., Catalli, K., Hustoft, J., Kubo, A., Prakapenka, V. B., Caldwell, W. A. & Kunz, M. (2008). *Proc. Natl Acad. Sci. USA*, **105**, 7383–7386.
- Stackhouse, S. & Brodholt, J. P. (2007). *The High-Temperature Elasticity of MgSiO<sub>3</sub> Post-perovskite*. In *Post-perovskite: The Last Mantle Phase Transition*, edited by K. Hirose, J. P. Brodholt, T. Lay & D. Yuen, Geophysical Monograph 174. Washington, DC: American Geophysical Union.
- Sugahara, M., Yoshiasa, A., Yoneda, A., Hashimoto, T., Sakai, S., Okube, M., Nakatsuka, A. & Ohtaka, O. (2008). *Am. Mineral.* **93**, 1148–1152.
- Tateno, S., Hirose, K., Sata, N. & Ohishi, Y. (2009). *Earth Planet. Sci. Lett.* **277**, 130–136.
- Toby, B. H. (2001). *J. Appl. Cryst.* **34**, 210–213.
- Trønnes, R. G. (2010). *Miner. Petrol.* **99**, 243–261.
- Tsuchiya, J., Tsuchiya, T. & Wentzcovitch, R. M. (2005). *J. Geophys. Res.* **110**, B02204.
- Vočadlo, L., Knight, K. S., Price, G. D. & Wood, I. G. (2002). *Phys. Chem. Miner.* **29**, 132–139.
- Wallace, D. C. (1998). *Thermodynamics of Crystals*. New York: Dover.
- Wood, I. G., Knight, K. S., Price, G. D. & Stuart, J. A. (2002). *J. Appl. Cryst.* **35**, 291–295.